2011

MODELING AND ANALYSIS OF AC CONDUCTION EFFECTS IN ALUMINUM & COPPER-ROTOR INDUCTION MACHINES AND DEVELOPMENT OF A NOVEL VOLTAGE REGULATION SCHEME FOR DISTRIBUTED WIND POWER GENERATION

Lakshmi Varaha K. Iyer
University of Windsor

MODELING AND ANALYSIS OF AC CONDUCTION EFFECTS IN ALUMINUM & COPPER-ROTOR INDUCTION MACHINES AND DEVELOPMENT OF A NOVEL VOLTAGE REGULATION SCHEME FOR DISTRIBUTED WIND POWER GENERATION

by

Lakshmi Varaha Iyer

A Thesis
Submitted to the Faculty of Graduate Studies
through Electrical Engineering
in Partial Fulfillment of the Requirements for
the Degree of Master of Applied Science at the
University of Windsor

Windsor, Ontario, Canada
2011

Modeling and Analysis of AC conduction Effects in Aluminum- and Copper-Rotor Induction Machines and Development of a Novel voltage Regulation Scheme for Distributed Wind Power Generation

by
Lakshmi Varaha Iyer

Approved By:

_____

D. Ting, Outside Department Reader
Mechanical, Automotive and Material Engineering

_____

K. Tepe, Departmental Reader
Department of Electrical and Computer Engineering

_____

N. Kar, Advisor
Department of Electrical and Computer Engineering

_____

R. Rashidzadeh, Chair of Defense
Department of Electrical and Computer Engineering

September 19, 2011

AUTHOR'S DECLARATION OF ORIGINALITY

I hereby certify that I am the sole author of this thesis and that no part of this thesis has been published or submitted for publication.

I certify that, to the best of my knowledge, my thesis does not infringe upon anyone's copyright nor violate any proprietary rights and that any ideas, techniques, quotations, or any other material from the work of other people included in my thesis, published or otherwise, are fully acknowledged in accordance with the standard referencing practices. Furthermore, to the extent that I have included copyrighted material that surpasses the bounds of fair dealing within the meaning of the Canada Copyright Act, I certify that I have obtained a written permission from the copyright owner(s) to include such material(s) in my thesis and have included copies of such copyright clearances to my appendix.

I declare that this is a true copy of my thesis, including any final revisions, as approved by my thesis committee and the Graduate Studies office, and that this thesis has not been submitted for a higher degree to any other University or Institution.

ABSTRACT

Centralized generation is being supplemented or replaced fast by distributed generation, a new way of thinking about electricity generation, transmission and distribution. Understanding the significance and prospects of self-excited induction generators (SEIGs) in distributed wind power generation (DWPG), this thesis exclusively presents the following:

1) A dynamic model of SEIG developed using the conventional two-axis transformation technique, commonly known as Park's transformation.
2) A developed electromagnetic model representing the AC conduction effects in the rotor bars of the machine to see the significance of incorporating these effects into the conventional two-axis model of the SEIG (improved mathematical model).
3) A comprehensive study of commercially available niche copper-rotor induction motor (CRIM) and conventional aluminum-rotor induction motor (ARIM) to be used as induction generators in the above application.
4) An experimental three phase short-circuit fault analysis in SEIGs for DWPG.
5) A novel low-cost embedded system based on Daubechies wavelet transforms and swarm intelligence technique for voltage regulation and fault detection in the above application.

DEDICATION

To
My Beloved Grandfather
Late Sri. K. L. V. Iyer

My Beloved Grandmother
Smt. Vijayalakshmi

My Beloved Mother and Father
Smt. Jaya Krishnan and Sri Krishna Iyer

& finally
My Beautiful sister
Sneha

ACKNOWLEDGEMENTS

First of all, my heartfelt gratitude to the almighty who has been driving me all through my career and now in writing this Thesis and sent me his blessings through like minded people who guided me to achieve a Masters Degree in Electrical Engineering which I thought was out of my reach.

More than the degree and the status that comes along, it is the knowledge and the happiness I gained over the last two years which gives me immense satisfaction of achieving something in life. I thank my late grandfather who would have been the happiest person to see me turn into what I am today, my family who blessed me and taught me to survive any hurdles and gave me the courage and taught me that nothing is impossible. They stood by me as I went about achieving my goal. I am also greatly indebted to my Mentor Sri S. Vaidhyasubramaniam without whose help, advice and sincere interest I would not have come to the University of Windsor. WE share this success.

I was just wet clay when my supervisor Dr. Narayan Kar saw me and predicted what I would be and showed me the way successful people are made of by constantly nurturing and motivating me. I still remember, he wanted me to be a 'motor man' right from the first day I joined. I thank him for instilling that confidence in me and hope I have lived up to his expectations. I wouldn't have been into research and obtained the satisfaction of engineering without him. Just a mere 'THANK YOU' to him would not be enough. I would like to express gratitude to my other thesis committee members, Dr. David Ting and Dr. Kemal Tepe. Their valuable suggestions and constructive advice have indeed ignited me to think 'out of the box' and go 'why' or 'why not'. My sincere thanks to both of them for taking their time to participate in the seminars, review the draft copies and provide constructive criticism.

I would like extend special thanks to Ms. Xiaomin Lu, my research partner and a good friend, who closely worked with me teaching me not just engineering or research but how hard work and how dedication pays off in life. She is a dynamic team player who works like a horse and sleeps like an owl.

I would also like to personally thank Dr. Kaushik Mukherjee who seamlessly nurtured me and supported me and taught me what in-depth research is. He was like a physician who treated me with ‘many’ and ‘any’ problems at any time of the day. He can be named an ATM (Any time Mentor).

Anas Labak is another fine gentleman I would like to thank. He helped me in everything and anything from research to personal life. My hearty thanks to him.

By default, I would always thank one of my teachers Sri G. M. Venkatesh, who was very influential in my life, as he moulded me right from my ninth grade upto my twelfth grade to be successful person in the competitive world. My heartfelt thanks to you Sir.

TABLE OF CONTENTS

LIST OF TABLES

LIST OF FIGURES

NOMENCLATURE

B	: Magnetic flux density
δ	: Skin depth
E	: Electric field intensity
ε	: Permittivity
f	: Frequency of induced current
h	: Height of the bar
H_{s1}, H_{s2}	: Magnetic field intensity
I	: Current in the rotor bar
J	: Current density
σ	: Conductivity of the material
μ	: Absolute magnetic permeability
w	: Width of the bar
ω	: Angular speed
l	: Length of the bar
K_r	: Resistance coefficient
K_l	: Inductance coefficient
R_{r_skin}	: Skin effect coefficient of resistance
L_{lr_skin}	: Skin effect coefficient of inductance
R_{r0}	: Original rotor resistance
L_{lr0}	: Original rotor inductance
R_{r_eff}	: Effective resistance of rotor
Llr_eff	: Effective inductance of the rotor
Cr_prox	: Multiplication factor of rotor resistance
Cl_prox	: Multiplication factor of rotor inductance

1.0 INTRODUCTION

1.1. Introduction to Distributed Wind Power Generation and Induction Generators

Over the years, energy policy in Canada has emphasized large centralized electricity generation and long-distance, high-voltage transmission from centralized sources such as large-scale hydro, coal, natural gas and nuclear power plants. This centralized energy infrastructure is becoming more challenging as demand for clean, reliable and affordable electricity generation grows. North America's centralized grid system stressed to its limits [1] has become vulnerable and increasingly brittle [2]. Over-reliance on large, polluting and expensive generation and transmission is no longer an option that Canadians would endorse. Hence, renewable energy sources are rapidly becoming a key contributor to Canada's electricity supply mix. As the nation's energy infrastructure ages, moving towards clean and inexhaustible sources of electricity is becoming a precondition of Canada's continued economic success in a competitive global market. Social, health and environmental constraints are fuelling a shift in national and regional energy policy, not only in Canada, but around the world. Distributed generation is the answer for the above issues.

Distributed generation refers to a variety of power-generating modules that can be combined with load management and energy storage systems to improve the quality and/or reliability of the electricity supply. They are "distributed" because they are placed at or near the point of energy consumption, unlike traditional "centralized" systems, where electricity is generated at a remotely located, large-scale power plant and then transmitted down power lines to the consumer.

Implementing distributed energy can be as simple as installing a small, stand-alone (autonomous) electricity generator to provide backup power at an electricity consumer's site. Or it can be a more complex system, highly integrated with the electricity grid and consisting of electricity and thermal generation, energy storage, and energy management systems. Consumers sometimes own the small-scale, on-site power generators, or they may be owned and operated by the utility or a third party.

Distributed energy encompasses a wide range of technologies including wind turbines, solar power, fuel cells, micro-turbines, reciprocating engines, load reduction technologies, and battery storage systems. The effective use of grid-connected distributed energy resources can also require power electronic interfaces and communications and control devices for efficient dispatch and operation of generating units.

Diesel- and petrol-fueled reciprocating engines are one of the most common distributed energy technologies in use today, especially for standby power applications. However, they create significant pollution (in terms of both emissions and noise) relative to renewable energy sources, and their use is actively discouraged by many municipal governments. As a result, they are subject to severe operational limitations not faced by other distributed generating technologies.

Furthermore, distributed energy technologies are playing an increasingly important role in the nation's energy portfolio. They can be used to meet peaking power, backup power, remote power, power quality, as well as cooling and heating needs. Distributed energy also has the potential to mitigate congestion in transmission lines, reduce the impact of electricity price fluctuations, strengthen energy security, and provide greater stability to the electricity grid. Distributed power generators are small compared with typical central-station power plants and provide unique benefits that are not available from centralized electricity generation. Many of these benefits stem from the fact that the generating units are inherently modular, which makes distributed power highly flexible. It can provide power where it is needed, when it is needed. And because they typically rely on renewable resources, the generators can be quieter and less polluting than large power plants, which make them suitable for on-site installation in some locations. The use of distributed energy technologies can lead to improved efficiency and lower energy costs, particularly in combined cooling, heating, and power (CHP) applications. CHP systems provide electricity along with hot water, heat for industrial processes, space heating and cooling, refrigeration, and humidity control to improve indoor air quality and comfort [3].

The growing popularity of distributed energy is analogous to the historical evolution of computer systems. Whereas we once relied solely on mainframe computers with outlying workstations that had no processing power of their own, we now rely primarily

on a small number of powerful servers networked with a larger number of desktop personal computers, all of which help to meet the information processing demands of the end users.

Wind power is becoming increasingly popular and is the fastest growing generation form because of its promising potentials for development. Government incentives have been successful, and the efficiency, longevity, and the overall quality of wind turbines have been constantly increasing. Residential wind turbines (producing 100 kW or less) have become a growing market area, as people are trying to reduce their dependency on the conventional power grid.The quality of Canada's wind resource is as good as or perhaps even better than any of the world's leading wind energy producing nations such as Germany, Spain and the United States. With abundant land mass and lengthy coastlines, Canada has top quality wind sites. Canada's total electrical demand could be met by tapping the wind potential of just one quarter of a percent of its land mass. Canadian Wind Energy Association (CanWEA), believes that wind energy can satisfy 20 percent of Canada's electricity demand by 2025. Achieving this vision will pay huge dividends such as adding 55 GW of clean generating capacity that will strengthen electrical grids and head off potential power shortages, thus stabilizing electricity prices and cutting Canada's annual greenhouse gas emissions by 17 Megatonnes [4].

The residential or distributed wind generators wind turbines use permanent magnet or self-excited generators to supply small demands effectively. A self-excited induction generator (SEIG) is an ideally suited electricity generating system for island operation of WDG as it becomes tedious and highly expensive to lay transmission lines over or under water, through mountainous areas and across long distances. A stand-alone SEIG driven by wind turbine is capable of supplying power to domestic, industrial and agricultural loads, particularly in the remote and hilly areas where conventional grid supply is not available. Installation of SEIG reduces the high maintenance and installation costs as large amounts of metal and raw material use can be minimized, infrastructure and transmission losses which occur when regular power grids or transmission lines are installed.

Self-excitation in induction machines with capacitors at their stator terminals, although known for more than half a century, is still a subject of considerable attention. Interest in

this topic is primarily due to the application of SEIGs in distributed wind power generation (DWPG). Over the years SEIG has emerged as an alternative to the conventional synchronous generator for such applications [5].

1.2. Case Studies of Distributed Wind Power Generation in North America

Selected case studies from [6] and [7] show some examples of isolated wind farms in Canada. Ramea Island, about 10 km off the south coast of Newfoundland, Canada, which is home to approximately 700 inhabitants, used one or more of three installed 925 kW diesel generators, with an average fuel efficiency of around 4 kWh/litre, to meet its electricity requirements. The latest island wind farm installed there produces around 10% to 13% of the 4.3 GWh consumed annually by the community, thus reducing the amount of fuel purchased for diesel generators. The island wind farm at Prince Island, Sault Ste. Marie in Ontario, Canada, produces 534 GWh per year, with 189 MW of installed capacity. In 1992 and 1993, the Yukon Energy Corporation of Canada installed a 150 kW wind energy generation system on Haeckel Hill, a shoulder of Mt. Sumanik, at an altitude of 1,430 m, approximately 750 m above the valley floor where the territory's capital, Whitehorse, is located. The Whitehorse grid, which is isolated from Canada's national electrical grid, also hosts 0.8 MW wind turbine capacity, provided at Haeckel Hill. A small stand-alone system installed in Southern Alberta allows a farm to operate independently off the grid. The farm had been connected to the grid, but the owner wished to have the farm autonomously powered, to reduce the environmental impact on his farm and home energy use. The farm's wind energy system supplies power to a residence for a family of four, a machine shop, a water well and yard lights. The rolling prairies of Alberta, between Calgary and Red Deer, are one of the most productive agricultural areas in Western Canada. A wheat farmer, who wanted independence from the electric utility, purchased a 10 kW wind turbine to supply all of his power requirements. The Trochu Wheat Farm was already connected to a power grid, but the farmer's goal was a stand-alone system that would survive inflation and have less environmental impact in comparison to the coal used to produce electricity for the grid.

In the USA, a home built near Ward, Colorado (at an elevation of 9,000 feet), has been

off-grid since it was built in 1972. When the house was built, the nearest utility was over a mile away, and it would have cost between $60,000 and $70,000 to connect to the utility lines. The owners decided to install a hybrid electric system powered by wind, solar, and a generator for a cost of about $19,700. Electric appliances in the home include television, stereo, two computers, toaster, blender, vacuum cleaner, and hair dryer. The largest electric loads are created by a well pump and washing machine [8].

1.3. Background Literature on Aluminum- and Copper- Rotor Induction Machines

As pointed out above, over the last decade, there has been a growing concern over the depletion of fossil fuels and more light has been shed on the usage and development of electric motors in different fields of application like hybrid electric vehicles and wind power generation. People who feel the heat of the future will strive to be in possession of a highly reliable motor. To maximize the reliability without overspending, induction machines need to be properly matched to the specific application. With this consideration, the choice between various rotor constructions needs to be evaluated. Higher efficiency electrical machines can reduce dependence on oil; lower greenhouse gas emissions and help the industry stay economically competitive by reducing energy costs. Millions of induction machines are sold in the world annually [9].

Conventional induction motors use less efficient aluminum rotors because fabrication by pressure die casting is a well established and economical method. Conventional wisdom states that copper conductors are the most reliable and outperform their aluminum counterparts, since the electrical conductivity of copper is 60% more than aluminum. Recent developments in the die casting process that produces copper rotors can easily increase the machine's efficiency by up to 2.1% [10]. Air pollution would also decrease as a direct result of reduced energy consumption. Use of copper rotors can also reduce motor operating temperatures by 5^{o}C to 32^{o}C [11]. As a general rule, for every 10^{o}C increase in the motor operating temperature, the insulation life of the motor is halved. Therefore, this data indicates that the lifetime of motors using copper rotors may be extended by 50% or more, with proper maintenance.

Recently, four 520 V, 140 hp induction machines with die cast copper rotors powered

the latest generation of US army severe duty hybrid electric vehicles. These machines were manufactured by Reliance Electric and it is stated that the die cast copper rotor technology was the only way they could meet the rigorous military requirements for weight, size and performance. It is also mentioned that, since copper is a better conductor of electricity and has lower resistance; copper rotors can be smaller, run cooler and have a higher power density. Hence, copper rotors may improve the efficiency of the system and result in a more fault tolerant system [12].

The nameplate efficiency of a practical, in-service, 15 hp, 1,800 rpm aluminum-rotor induction machine today is about 89.5%, which is below the 1997 Energy Policy Act standard of 91%. As demonstrated by many other researchers, the adoption of copper rotors should bring efficiencies to the 94 to 96% range exceeding the requirements of today's NEMA premium efficiency motor, nominally 93% [13]. In addition, analyses by motor manufacturers have shown that copper rotors can be employed to reduce overall manufacturing costs at a given efficiency or to reduce motor weight, depending on which attribute the designer chooses to emphasize. The potential energy savings achievable through the use of copper rotors is substantial. The U.S. Department of Energy reports that motors above 1/6 hp use about 60% of all electricity generated in the United States and the medium power motors (1 to 25 hp) are the favored candidates for conversion to copper rotors [14]. In Canada alone, 1 percentage increase in the motor electrical energy efficiency would save roughly $200 million and as a result, 0.5 million barrels of oil annually. As Canada and the world move rapidly towards increased dependence on wind power generation, aluminum and copper can play an important role in the rotor construction of SEIG [15].

1.4. Previous research performed on SEIGs

The phenomenon of self excitation in induction machines has been known for more that 70 years. In this section works carried out previously in the area of self excited induction generators using squirrel cage rotors, especially in the field of wind power application are reviewed. Research is previously performed in the following areas:

- Modelling
- Determination of minimum capacitance required for excitation

- Voltage build up
- Steady state analysis of isolated induction generators
- Steady state analysis of generators connected to the grid
- Parallel operation of induction generators
- Voltage regulation and control
- Transient analysis.

Like the induction motors, induction generators are generally classified on the basis of rotor construction. They can be wound rotor or squirrel cage type. Wound rotor induction generators are generally used as Doubly Fed Induction Generators (DFIG) while squirrel cage rotors are used as grid connected or isolated type induction generators. Depending on the type of prime movers and their control mechanism induction generators can be broadly classified as [16].

- Constant Speed Constant Frequency
- Variable Speed Constant Frequency
- Variable Speed Variable Frequency

For variable speed corresponding to the changing speed of the prime mover, SEIG can be conveniently used for loads which are essentially frequency insensitive. This scheme is gaining importance for stand-alone wind power applications.

Using the d-q reference frame model of a three phase induction generator, the transient performance can be studied. For transient analysis, the d-q reference frame model of the SEIG, based on generalized machine theory has been used [16]–[21]. The conventional three *a, b* and *c* reference frames of the machine are transformed into two reference frames, *d* and *q* and all the analysis are carried out using rotor, stationary or synchronous reference frame [22], [23]. The results are then transformed back to the actual three reference frames. If the time varying terms in the d-q axis model are ignored, the equations then represent only the steady state conditions [24]. Most of the transient studies of induction generators are related to voltage build-up due to self excitation and load or speed perturbation. Symmetrical component concepts have been used to analyze unbalanced systems using positive and negative sequence equivalent circuits [25]. Study of long-shunt and short-shunt configurations on dynamic performance of an isolated

SEIG, and the analysis of SEIG feeding an induction motor has been done by other authors [16] using d-q frames of reference.

In the steady state analysis, per phase equivalent circuit of the SEIG has been developed from the classical model of an induction machine. The main feature that distinguishes an induction machine from other electrical machines is that, like the transformer, the secondary currents are created totally by magnetic induction. In an isolated power system consisting of the induction generator, the excitation capacitor and load, both the terminal voltage and frequency are unknown and have to be computed for a given speed, capacitance and load impedance. Usually there are four unknowns, reactance of the excitation capacitor X_c, magnetizing reactance X_m, per unit frequency a, and per unit speed b. Early articles on this subject emphasised on evaluating the value of the minimum capacitance required for self excitation. Two different methods of solution have been used namely, the loop impedance method [26]-[29] and the nodal admittance method. Both these methods used the classical model of the induction machine. In the loop impedance method, for a given load and speed, two non-linear simultaneous equations in per unit frequency, a and magnetizing reactance, X_m are obtained by equating the real and imaginary terms of the complex loop impedances respectively to zero. The generator performance can then be evaluated by solving these equations. An alternative method of solution using the steady-state equivalent circuit is by considering the nodal admittance method described in [30]-[32].

By means of loop impedance or nodal admittance method technique, equations are obtained and then separated into its real and imaginary parts to solve for the per unit frequency a and then for capacitive reactance X_c or magnetizing reactance, X_m. Chan [30] has proposed an iterative technique by assuming some initial value of a. The second technique proposed by Chan [33] is based on the nodal admittance method. Here the symbolic programming using Maxima (software of MACSYMA) is employed for the derivation and solution of the high-order polynomial. Other authors have used Newton-Raphson method to solve for the unknowns [34]. Harrington [35] and Malik et al [29] have shown that the minimum capacitance requirement of an SEIG is inversely proportional to the speed and maximum saturated magnetizing reactance. Calculation to predict both minimum and maximum values of capacitance required for self-excitation

based on eigenvalues and eigenvalue sensitivity analyses has also been reported in [36] and [37]. Harrington [35] has proposed a method based on the analysis of the complex impedance matrix of the induction generator when loaded with a general inductive load.

1.5.Research objectives of this thesis

a) *Development of Analytical model of SEIG for improved accuracy through incorporation of AC conduction effects in the rotor-bar of SEIG*

The analysis of the performance of induction machines due of variation of frequency has been reported by several authors [38]–[41]. The frequency of the stator voltage is dependent on rotor speed, magnitude of the excitation capacitance and load [39]. The variation of stator frequency has a profound effect on the rotor parameters. This in turn influences the performance of the machine. Otherwise, in case of a SEIG, the frequency of current in the rotor is affected by the varying load and speed of the wind turbine. The resulting high frequency of current gives rise to a phenomenon called the "Skin Effect". Skin effect plays an important role in the performance of the SEIG due to higher current density at the surface of the rotor bars [42].

Until now, a conductor subjected to skin effect has been considered to be isolated and outside the influence of any magnetic field, except its own. This assumption is no longer valid when another conductor is in its vicinity; a further distortion in current density occurs due to the interaction of the magnetic field of adjacent rotor conductors. The magnetic flux of one bar induces an e.m.f. in the adjacent conductors, increasing the non uniformity of current density. If two conductors in close proximity carry currents in opposite directions, their electromagnetic fields are opposed to one another and tend to force the conductors apart. There exists a decrease in flux linkages around the adjacent parts of conductors and an increase around the outer parts of the same conductor; which results in a concentration of current in the adjacent parts, where back e.m.f. is at a minimum. If the current flows in the same direction, it tends to be concentrated in the remote parts of the conductors. This is known as the "Proximity Effect" which also increases the resistance of the conductors, hence, the Joule losses [43].

Since, the rotor bars can be of copper or aluminum, the performance of these materials under the influence of proximity effect is determined in this thesis. Although,

copper is a better substitute for aluminum in general, we can increase the efficiency of copper-rotor induction generators if these effects are carefully dealt with. As reported in [44], these effects have been the only concern in further increasing the efficiency of copper-rotor machines and the higher conductivity of copper allows the rotor designer to use these effects to tailor the behavior of the rotor to improve machine performance. Research conducted in [42]-[46] show that the proximity effect is significant in the active length of the conductors and the impact of Joule losses in the design of rotor conductors is large due to the dissipating energy, causing thermal problems.

The research on aluminum- and copper-rotor SEIGs considering skin and saturation effect has been demonstrated in [47]. However, the research performed on SEIGs till date does not show their performance under the influence of proximity effect. Chapter 2.0 of this thesis explains the analytical model of a SEIG developed considering both skin and proximity effects. The influence of proximity effect on the performance of both the machines is analyzed. Exclusive qualitative analysis of real power, reactive power and power loss due to proximity effects at different static loads is accomplished in detail for both the machines. The simulated results are experimentally verified for two industrial 7.5 hp aluminum- and copper-rotor induction machines.

b) *Study of commercially available niche CRIM and conventional ARIM to be used as self-excited induction generators in distributed wind power generation*

A commercially available induction motor to the general consumer can be used as a SEIG. It is readily available to the consumer for any application (motoring/ generating). Buying a generator directly might be expensive as low rating generators for small wind farms are not mass produced. However, the performance of these motors as SEIGs can be only judged based on their voltage regulation, frequency regulation and VAR requirement characteristics at different operating conditions. Recently, due to the growing cost and complexity of voltage regulating schemes the need has been felt to develop an economical regulating scheme and also minimally modify the induction motor to improve its generating characteristics and reduce its dependency on regulating schemes.

However, conventional induction motors can be efficiently used as SEIGs if they are either minimally redesigned for the same application or by choosing the best out of the available induction machines through suitability analysis. Chapter 3.0 of this thesis

exclusively studies the suitability of the relatively newer copper-rotor induction motor (CRIM) and the conventional aluminum-rotor induction motor (ARIM) for use as a SEIG in DWPG. Experimental investigations are performed on two 7.5 hp CRIM and ARIM and the measured results are corroborated by discussions.

c) *A novel low-cost embedded system based on Daubechies wavelet transforms and swarm intelligence technique for voltage regulation in SEIGs for distributed wind power generation.*

Major challenges in an SEIG are its poor voltage and frequency regulation, since there is no separate DC excitation system. As a load is applied, the VAR supplied by the capacitance of the parallel combination of the excitation capacitance and the connected load must match the VAR demanded by the machine as dictated by the magnetizing curve. In other words, the VAR, required by the machine to maintain self-excitation and the load must be provided solely by the excitation capacitor. Consequently, as the load is increased, there is a decrease in magnitude of the terminal voltage and frequency. Various techniques for improving voltage regulation such as a switched capacitor scheme, electronic load controllers, variable VAR controllers and other solid state controllers are reported in the literature [48]-[55], which improve the performance of a SEIG significantly, but involve complex and expensive control hardware.

Understanding the significance and the need for a low-cost incomplex voltage regulation scheme in a SEIG for distributed wind power generation, chapter 4.0 proposes a part of an exclusive control scheme involving the developed particle swarm optimization (PSO) and the discrete wavelet transforms (DFT) for voltage regulation.

Chapter 3.0 illustrates the importance of this research and the need for the developed voltage regulation (VR) scheme. Chapter 4.0 explains in length the modelling and implementation of the developed wavelet/PSO based module. It also elicits the step by step process involved in designing the module along with the calculated and experimental results captured at every step of the design. A comprehensive investigation of the developed algorithm has been performed through a developed computer program and an experimental set-up consisting of a low-end embedded system and switched capacitance based voltage regulator. However, the developed VR scheme is recommended to be

integrated with a static synchronous compensator (STATCOM) for better resolution and performance in voltage regulation. Further background study on the developed schemes and mathematical models will be provided in their respective sections.

d) *An experimental three phase short-circuit fault analysis in SEIGs for distributed wind power generation*

One of the challenges in an SEIG system is fault detection in the system. Faults across the high-voltage terminals of the generator lead to economic losses and power outages. A study performed by the Electric Power Research Institute (EPRI) estimated the cost of power interruptions in the US at $119 billion per year [56]. Forced outages are the primary concern of the remote area consumer for causing economic duress. The SEIG is attractive for DWPG as the terminal voltages of the system collapse during short-circuit faults and hence, the excitation of the machine is cut-off driving the machine to just run freely at the wind turbine rotor speed. However, it is necessary for the fault to be detected and communicated to the operator in order to resume operation after fault inspection and clearance.

Generally, when power line fault occurs, the conventional devices such as auto-reclosing circuit breakers or over-current sensors are used to detect the current amplitudes and break the circuit for power transfer termination and safeguard the generator and load. Also, the detection can be communicated to the operator based on the post-fault information gathered.

However, in the case of a SEIG, during three-phase short circuit condition the voltage across the capacitor banks falls to zero and hence the stator current drops to zero. Here the machine is protected from faulty currents as the machine stops generating until the fault is cleared due to zero voltage build up across its terminals. The conventional fault detection devices mentioned above cannot be employed to detect the fault as the amplitudes of currents do not rise for a period of time. Hence, fault detection is necessary through other methods. Fast and accurate fault detection will render immediate corrective action. Thus, it is of vital importance to rapidly detect and identify power system faults, assist the task of repair and maintenance, and reduce the economic effects of power interruption.

Hence, chapter 5.0 of this thesis shows this meritorious self protecting mechanism of the SEIG system through fault analysis and thus its usability in distributed generation. Also, the wavelet based transient detection scheme which is developed in this thesis for voltage regulation, explained in later chapters, can be used for fault detection and classification through conditional threshold selection, hence making the wavelet based module a dual purpose module for voltage regulation and fault detection in distributed wind power generation.

1.6. References

[1] http://www.ornl.gov/info/ornlreview/v38_1_05/article11.shtml,"More power to the grid," Oak Ridge National Lab. Review, 38, 2005.

[2] A. B. Lovins, K. E. Data, T. Feiler, K. R. Rabago, J. N. Swisher, and A. Lehmann, "Small is profitable: The hidden economic benefits of making electric resources the right size," 2002.

[3] http://www.nrel.gov/learning/eds_distributed_energy.html,"Distributed Energy.

[4] http://www.canwea.ca, "Wind vision 2025: Powering Canada's Future," November 2010.

[5] B. Singh, M. Singh, and A. K. Tandon, "Transient performance of series-compensated three phase self excited induction generator feeding dynamic loads," *IEEE Trans. on Industry Applications*, vol. 46, no. 4, July/ August 2010.

[6] www.nrcan-rncan.gc.ca, Natural Resources of Canada, Case Studies, "390 kW - Isolated-grid/Canada," February 2009.

[7] http://www.smallwindenergy.ca, "Small wind case studies and success stories," Canadian wind energy association.

[8] www.energy.gov, Small Wind Electric Systems, A US consumer Guide.

[9] W. R. Finely and M. M. Hodowanec, "Selection of copper vs. aluminum rotors for induction motors," in *Proc. IEEE Petroleum and Chemical Industry Conference*, 2000.

[10] Copper.org, CDA Press Releases, "Building a better electrical motor," January 2005.

[11] Copper.org, CDA Press Releases, "Die-cast copper rotor improves motor efficiency motor," January 2005.

[12] Copper.org, CDA Press Releases, "Copper Motor rotors boost performance of Army trucks," January 2007.

[13] J. G. Cowie, D. T. Peters, and D. T. Brender, "Die-cast copper rotors for improved motor performance," in Proc. IEEE Pulp and Paper Industry Technical Conference, 2003.

[14] Canadian Copper and Brass Development Association, "Wind power and copper in Canada," No. 154, 2006.

[15] Canadian Copper and Brass Development Association, "Technology transfer report - The die cast copper rotor motor," April 4, 2004.

[16] R.C. Bansal, "Three Phase Self Excited Induction Generator: An overview," *IEEE Transaction on Energy Conversion*, Vol.20, No. 2, pp. 292-299, Jun. 2005.

[17] P.C. Krause and C.H. Thomas, "Simulation of Symmetrical Induction Machinery," *IEEE Transaction on Power Apparatus and Systems*, Vol. PAS-84, No. 11, pp. 1038-1053, Nov. 1965.

[18] L. Wang and C.H. Lee, "Dynamic Analysis of Parallel Operated Self-Excited Induction Generators feeding an Induction Motor Load," *IEEE Transaction on Energy Conversion*, Vol. 14, No. 3, pp. 479-486, Sep. 1999.

[19] R.H. Nelson, T.A. Lipo and P.C. Krause, "Stability Analysis of a Symmetrical Induction Machine," *IEEE Transaction on Power Apparatus and Systems*, Vol. 88, pp. 1710-1717, Nov 1969.

[20] E. Levi, "Application of the Current State Space Model in Analyses of Saturated Induction Machines," *Electric Power Research*, pp. 203-216. 1994.

[21] R. Djamila R and R. Toufik, "An approach for the Modeling of an Autonomous Induction Generator Taking into account the Saturation Effect," *International Journal of Emerging Electric Power Systems*, Vol. 4 No. 1, pp. 391- 2005.

[22] P.C. Krause, *Analysis of Electric Machinery and Drive Systems*, 2nd Edition, IEEE Press, 2002.

[23] O.I. Okoro, "Matlab Simulation of Induction Machine with Saturable Leakage and Magnetizing Inductances", *The Pacific Journal of Science and Technology*, Vol. 5, No. 1, pp. 5-15, Apr. 2003.

[24] D. Seyoum, "The Dynamic Analysis and Control of a Self-Excited Induction Generator driven by a Wind Turbine," Ph. D. Dissertation, The University of New South Wales, Australia, 1999.

[25] S. S. Murthy and S. Acharya, "Matlab Based Steady State Analysis of Self Excited Induction Generator," *The Fifth International Conference on Power Electronics and Drive Systems*, Vol. 1, pp. 749-753 Nov. 2003.

[26] S.S. Murthy, O.P. Malik and A.K. Tandon, "Analysis of Self-Excited Induction Generators," *Proceedings of IEE*, Vol. 129, Part C, No. 6, pp. 260-265, Nov. 1982.

[27] N.H. Malik and S.E. Haque, "Steady State Analysis and Performance of an Isolated Self-Excited Induction Generator," *IEEE Transaction on Energy Conversion*, Vol. EC-1, No. 3, pp.134-139, Sept. 1986.

[28] T.F. Chan, "Steady State Analysis of Self Excited Induction Generators," *IEEE Transactions on Energy Conversion*, Vol.9, No. 2, pp. 288-296, Jun. 1994.

[29] N.H. Malik and A.A. Mazi, "Capacitance Requirements for Isolated Self Excited Induction Generators," *IEEE Transaction on Energy Conversion*, Vol. EC-2, No. 1, pp. 62-68, Mar. 1987.

[30] T.F. Chan, "Analysis of Self-Excited Induction Generators Using an Iterative Method," *IEEE Transactions on Energy Conversion,* Vol. 10, No. 3, pp. 502-507 Sept. 1995.

[31] A.M. Eltamaly, "New Formula to Determine the Minimum Capacitance Required for Self-Excited Induction Generator," *IEEE 33rd Annual Power Electronics Specialists Conference*, Vol. 1 pp. 106-110, Jun. 2002.

[32] S. U Alghuwainem, "Steady-State Analysis of an Isolated Self-Excited Induction Generator supplying an Induction Motor Load," *IEEE Transaction on Energy Conversion*, Vol. 14, Issue 3, pp. 718-723, Sept. 1999.

[33] T.F. Chan, "Capacitance Requirements of Self-Excited Induction Generators," *IEEE Transactions on Energy Conversion*, Vol. 8, No. 2, pp. 304-311, Jun. 1993.

[34] S.S. Murthy and A.J.P. Pinto, "A Generalized Dynamic and Steady State Analysis of Self Excited Induction Generator (SEIG) Based on Matlab," *Proceedings of the Eighth International Conference on Electrical Machines and Systems*, Vol. 3, Issue , pp. 1933-1938, Sep. 2005.

[35] R.J. Harrington and F.M.M. Bassiouny, "New Approach to Determine the Critical Capacitance for Self-Excited Induction Generators," *IEEE Transactions on Energy Conversion*, Vol. 13, No. 3, pp. 244-249, Sep. 1998.

[36] L. Wang and C.H. Lee, "A Novel Analysis on the Performance of an Isolated Self-Excited Induction Generator," *IEEE Transactions on Energy Conversion*, Vol. 12, No. 2, pp. 109-117, Jun. 1997.

[37] L. Wang and J.Y. Su, "Determination of Minimum and Maximum Capacitance of an Isolated SEIG using Eigenvalue Sensitivity Approach," *Proceedings of International Conference on Power System Technology*, Vol.1, pp. 610-614, Aug. 1998.

[38] J. Langheim, "Modeling of Rotor Bars with Skin Effect for Dynamic Simulation of Induction Machines," Conference Record of the 1989 IEEE Industry Application Society Annual Meeting, Vol. 1, pp. 38-44, 1989.

[39] H. Kabbaj, X Roboam, Y. Lefevre and J. Faucher, "Skin Effect Characterization in a Squirrel Cage Induction Machine," Proceedings of the IEEE International Symposium on Industrial Electronics, Vol. 2, pp. 532-536, 1997.

[40] N. Erdogan, T. Assaf, R. Grisel and M. Aubourg, "An Accurate 3-phase Induction Machine Model Including Skin Effect and Saturations for Transient Studies," Sixth International Conference on Electrical Machines and Systems, pp. 646-649, 2003.

[41] O.I. Okoro, "Transient State Modeling of Asynchronous Generator with Skin Effect," The Pacific Journal of Science and Technology, Vol. 5, No. 2, pp. 63-71, 2004.

[42] K. Hafiz, G. Nanda, and N. C. Kar, "Performance analysis of aluminum and copper rotor induction generators considering skin and thermal effects," *IEEE Trans. on Industrial Electronics*, vol. 57, January 2010.

[43] J. D. Milburn, "Skin and proximity effects in heavy-current conductors," Student's Quarterly Journal, March 1969, pp. 172-180.

[44] Canadian Copper and Brass Development Association, "Technology transfer report - The die cast copper rotor motor," April 4, 2004.

[45] R. Wrobel, A. Mlot, and P. H. Mellor, "Investigation of end-winding proximity losses in electromagnetic devices," in Proc. XIX IEEE Inter-national Conference on Electric Machines, 2010.

[46] A. Ducluzaux, "Extra losses in high current conductors by skin and proximity effects," Schneider Electric-Cahier Technique no. 83, 1983.

[47] K. Hafiz, G. Nanda, and N. C. Kar, "Skin effect modeling of self excited induction generator in wind power application," in Proc. of IEEE Canadian Conference on Electrical and Computer Engg., May 2008.

[48] L. Wang and C. M. Cheng, "Selection of magnetizing curves for accurately simulating a three-phase self-excited induction generator feeding a single-phase load," IEEE Power Engineering Society Winter Meeting, vol. 1, no. 1, pp. 286-290, 2000.

[49] N. H. Malik and A. A. Mazi, "Capacitance requirements for self excited induction generators," IEEE Trans. on Energy Conversion, vol. 2, 1987.

[50] S. N. Mahato, S. P. Singh, and M. P. Sharma, "Capacitors required for maximum power of a self-excited single-phase induction generator using a three-phase machine," IEEE Trans. on Energy Conv., vol. 23, 2008.

[51] B. Singh, S. S. Murthy, and S. Gupta, "STATCOM based voltage regulator for self excited induction generator," IEEE Trans. Ind. Electronics, vol. 53, no.5, pp. 1437-1452, Oct. 2006.

[52] K. H. Youssef, M. A. Wahba, H. A. Yousef, and O. A. Sebakhy, "A new method for voltage and frequency control of stand-alone self excited induction generator using PWM converter with variable DC link voltage," in Proc. of American Control Conference, pp. 2486-2491, 2008.

[53] R. Bonert and S. Rajakaruna, "Self excited induction generator with excellent voltage and frequency control," Proc. Inst. Elect. Eng. Gen., Tran. and Dist., vol. 145, pp. 33-39, Jan. 1998.

[54] S. C. Kou and L. Wang, "Dynamic eigen-value analysis of a self-excited induction generator feeding an induction motor," in Proc. IEEE Power Engg. Society Winter Meeting, vol. 3, no. 1, pp. 1393-1397, 2001.

[55] S. C. Kou and L. Wang, "Steady-state performance of a self-excited induction generator feeding an induction motor," Journal of Electric Power Components and Systems, pp. 581-593, 2002.

[56] K. M. LaCommare and J. H. Eto, "Cost of power interruptions to electricity consumers in the United States (U.S.)," Ernest Orlando Lawrence Berkley National Lab., Env. Energy Technologies Division, Feb. 2006.

2.0 MODELING OF ALUMINUM- AND COPPER-ROTOR SEIGs INCORPORATING PROXIMITY EFFECT IN THE ROTOR BARS

2.1 Process of self-excitation and voltage build up in SEIGs

The phenomenon of self-excitation in induction machines has been known and studied for over several decades [1]. When an induction machine is connected to an AC source, a component of its stator current is used to build-up the air gap magnetic flux whether the machine works as a motor, brake or a generator [2]. If the machine operates as a generator, reactive power is required to build up the magnetic flux. This reactive power can be provided from the grid. In an isolated mode, this excitation can be provided by an external capacitor of appropriate value. In other words, to build up the voltage across the generator terminals, some means of excitation is required [3]. To achieve a given voltage level, the external capacitors must supply the required magnetizing current and hence the reactive power.

An induction generator without any external source, using capacitors can self-excite if there is a remnant magnetic flux in the machine core [4]–[5] or residual charge across the capacitor terminals. The residual magnetism in the field circuit produces a small voltage. That voltage produces a small capacitive current flow. This boosts up the voltage which further increases the capacitive current until the voltage is built up. Thus a three phase induction machine can be made to work as a self-excited induction generator provided capacitance connected across the stator terminals have sufficient charge to provide necessary initial magnetizing current [6]–[9]. In such a case, this phenomena is known as capacitor self excitation, and the induction machine is called Self Excited Induction Generator (SEIG).

In an induction machine with a capacitor connected across its terminals, if the effect of the small stator resistance R_s and stator leakage inductance L_{ls} are neglected, the equivalent circuit for no load excitation takes the form of a parallel LC circuit, where L represents the induction motor and C the excitation capacitor. Such a circuit can be excited at a given frequency with the least amount of energy when the currents in the inductor and capacitor are equal. Thus if an induction machine is driven by a prime

mover, and if the capacitor is charged it provides the exciting current required by the induction generator to produce a magnetic flux. The magnetic flux in the induction generator charges the capacitor to increase the terminal voltage. An increase in the capacitor voltage boosts up the excitation current to the generator to increase the flux which in turn increases the terminal voltage. In this way the voltage and current build up continues until the magnetizing inductance decreases to its saturated value and equilibrium point is attained. The process will continue until steady state is reached.

In order to estimate the level of saturation and the mutual inductance term at a particular operating condition require the representation of the magnetization curve of the induction generator under consideration. The magnetizing characteristic of an induction machine is a curved line. In the absence of saturation of the iron this line should ideally be straight. But due to saturation the line becomes curved beyond a certain excitation current. This curve represents characteristic at a particular rotor speed. If the magnetizing characteristic is obtained at a higher rotor speed, a steeper curve will be obtained as shown in Fig. 2.1. This figure shows the relationship between the size of the excitation capacitance, the rotor speed and generated voltage.

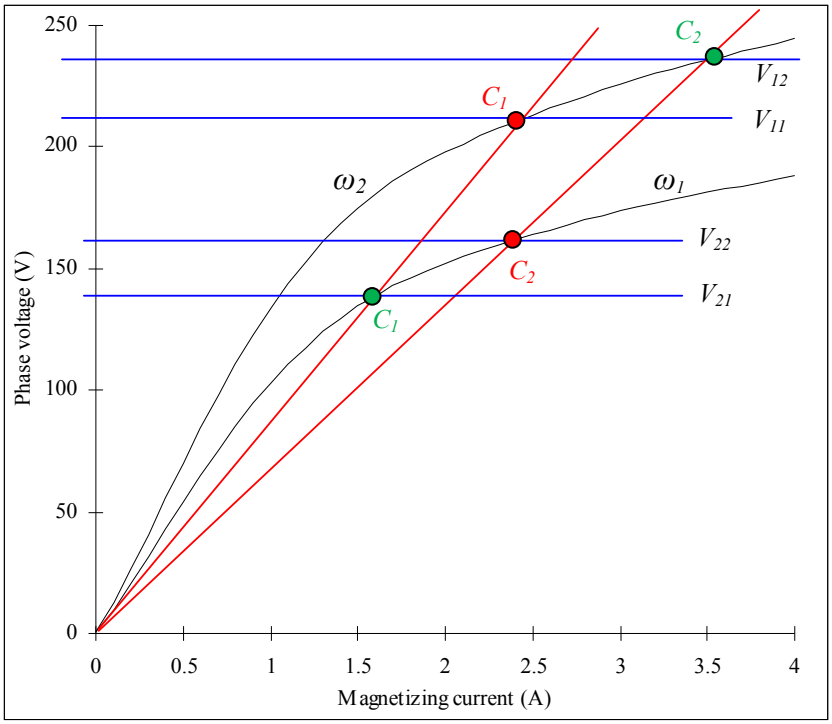

Fig. 2.1. V-I characteristics of an induction machine (shown in black) and excitation capacitor (shown in red) and the steady state voltage levels built-up shown using blue lines. $\omega_2 > \omega_1$, $C_1 < C_2$.

As the magnetising current produced by a capacitor is directly proportional to the voltage applied to it, the locus of the voltage and current relationship is a straight line. It can be seen from Fig. 2.1 that for each amount of capacitance there is a single point where the inductor and capacitor currents are equal. This is the intersection point of the magnetizing curve and the linear capacitor volt-ampere characteristic at the particular rotor speed at no load. At this point the voltage and current will oscillate at a certain peak value and frequency. Once self-excitation has been initiated, the open circuit voltage to which the machine will self-excite can be calculated i.e.V_{21} at a capacitance C_1 and rotor speed ω_1. If the capacitance is increased (from C_1 to C_2) a higher voltage, V_{22} will be generated at the same speed as the slope of the VI characteristics of the capacitor will be tilt towards the right with increasing value of C. Similarly, at a higher rotor speed, ω_2, higher voltages will be generated depending on the capacitance values.

At low magnetizing current where the magnetizing curve is practically linear, the intersection with the capacitor line is not well defined. This will result in poor flux stability and voltage regulation in this region. This is the minimum value of capacitance beyond which the machine will not maintain or build up excitation at all. Any value of capacitor lower than the minimum will result in loss of excitation if the machine is already generating or will not be able to initiate self excitation if the machine is starting.

It is necessary that some external energy source should be available to the rotor to supply the losses associated with the stator current. There must also be an initial charge on the capacitor or residual magnetism in the rotor iron to initiate the voltage and current to build up. As explained earlier, when the machine is driven by an external prime-mover, the remnant flux in the rotating rotor induces a small voltage in stator windings, which carries a leading current if suitable terminal capacitors are connected [11]. The reactive energy to excite the induction generator thus oscillates between the electric field of the capacitors and magnetic field of the machine [2]. This assists the core flux and causes an avalanche effect due to the differential voltage equal to the difference between induced voltage and capacitor voltage. The voltage rise thus continues till saturation sets in and steady state is reached. Saturation of the magnetic circuit is the main requisite for the stabilization of the voltage. As can be seen from Fig. 2.1, for a certain value of the excitation capacitor the slope of the V-I line will be such that it intersects the magnetic

saturation curve at a point. This point of intersection will be the steady state terminal voltage (V_{11}, V_{12}, V_{21} and V_{22}) and excitation current. If saturation is absent, the curve will essentially be a straight line and the two lines will not intersect. Consequently there will be no excitation.

The steady state performance characteristics of an isolated self-excited induction generator are influenced by the magnitude of the excitation capacitor and rotor speed. The terminal capacitor must have its value within a certain range to sustain self-excitation. If the value of the excitation capacitor is outside this range, self-excitation will not be possible [12]-[14]. As explained above, the capacitor in such a machine must have a minimum value, C_{min} for self excitation to take place. On the other hand in order to sustain operation, the terminal capacitor must also be below a certain maximum value C_{max} [13]. Both the minimum and maximum values are affected by the machine parameters, speed and load conditions.

2.2 Analytical Modeling of the SEIG using conventional two-axis model

Previous research performed on SEIG is mainly concerned with representing the machine by steady state models and the dynamic models. The steady state SEIG is modeled as per phase equivalent circuit. In this circuit the slip and angular frequency are expressed in per unit quantities. Previous authors have used either the loop impedance method [1]-[3] or the nodal admittance method [4]-[6] to analyze the machine performance. In the loop analysis technique the total loop impedance which includes the excitation capacitance is equated to zero. In the nodal admittance method the overall admittance of the SEIG at a certain node is set to zero. These methods give an algebraic expression for magnetizing reactance in terms of generator frequency and other machine parameters and speed. For the determination of the operating frequency a and magnetizing reactance X_m the real and imaginary parts of the sum of admittances of the rotor, magnetizing and stator branches are separately equated to zero. In these approaches there are usually four unknowns, the magnetizing reactance X_m, the excitation capacitance X_c, per unit frequency a and per unit speed b. Assuming values of any two, the other two are found by iteration process [4] or numerical solution. In both the loop and nodal

analysis a high order polynomial or a non-linear simultaneous equation is used where the general focus is to find the value of the capacitance required for self-excitation. Several researchers indicated that there is a minimum value of excitation capacitance to initiate self-excitation for a given speed and load condition [7] while some also exploited the maximum value of this capacitance [2], [5] beyond which excitation will not be maintained.

The d-q reference model using Park's transformation was proposed by Krause and Thomas [8]. This method was further extended by other authors [9]-[11] for dynamic analysis of induction machines. The non-linear differential equations that describe the dynamic performance of an induction machine in an arbitrary reference frame can be derived from the d-q equivalent circuits. To analyse the performance of an induction generator, differential equations describing the excitation capacitance and load are also taken into account. This method has been employed in this thesis to model the SEIG.

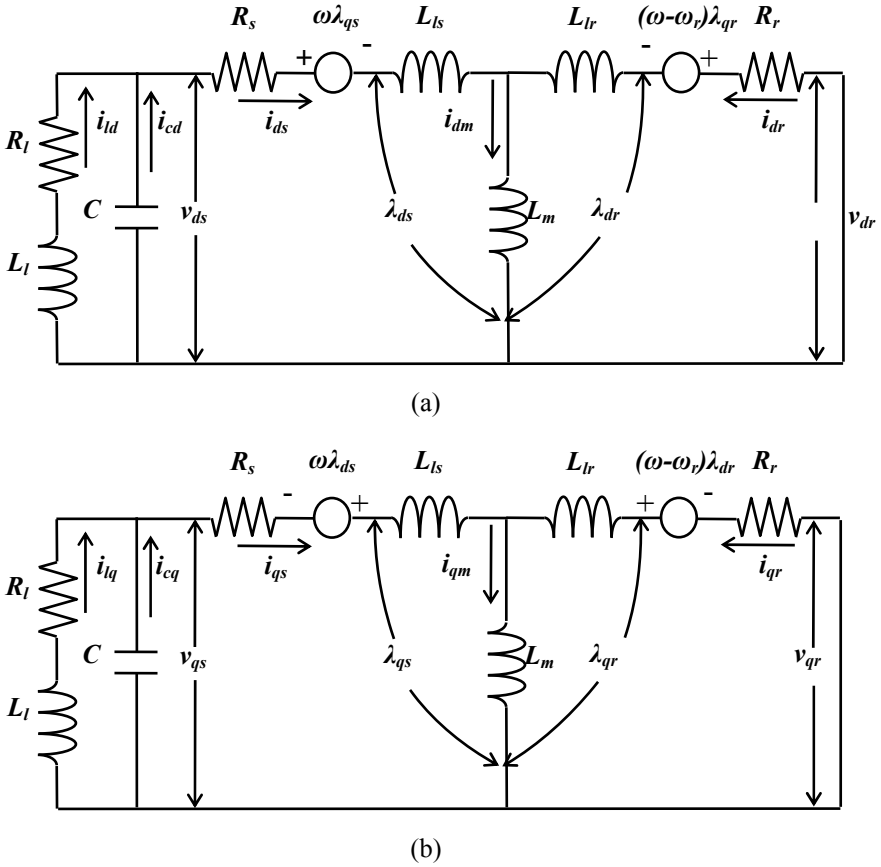

Fig. 2.2 Equivalent two-axis circuit of an SEIG. (a) d-axis. (b) q-axis.

The induction machine circuit diagram as presented in Figs. 2.2 (a) and (b), can be modeled using d-q axis reference frame. These figure show the direct and quadrature representation of a squirrel cage induction machine. It is the most commonly used transient state model in the d-q axis frames of reference [10]. The advantage of the d-q axis model is that it is a powerful tool for analyzing the dynamic and steady state conditions, thus providing a complete solution for any dynamics. For steady state analysis, the conventional model and the d-q reference are the same.

From the above figures the d-q axis stator and rotor voltages of an induction machine can be expressed in matrix notation as:

$$\begin{bmatrix} v_{qs} \\ v_{ds} \\ v_{qr} \\ v_{dr} \end{bmatrix} = \begin{bmatrix} R_s + pL_s & \omega L_s & pL_m & \omega L_m \\ -\omega L_s & R_s + pL_s & -\omega L_m & pL_m \\ pL_m & (\omega - \omega_r)L_m & R_r + pL_r & (\omega - \omega_r)L_r \\ -(\omega - \omega_r)L_m & pL_m & -(\omega - \omega_r)L_r & R_r + pL_r \end{bmatrix} \cdot \begin{bmatrix} i_{qs} \\ i_{ds} \\ i_{qr} \\ i_{dr} \end{bmatrix} \tag{2.1}$$

where $p = \frac{d}{dt}$ and

$$\left.\begin{aligned} L_s &= L_{ls} + L_m \\ L_r &= L_{lr} + L_m \end{aligned}\right\} \tag{2.2}$$

$$\left.\begin{aligned} \lambda_{qs} &= L_s i_{qs} + L_m i_{qr} \\ \lambda_{ds} &= L_s i_{ds} + L_m i_{dr} \\ \lambda_{qr} &= L_r i_{qr} + L_m i_{qs} \\ \lambda_{dr} &= L_r i_{dr} + L_m i_{ds} \end{aligned}\right\} \tag{2.3}$$

Equation (2.1) may be written as

$$\left[v_{dq} \right] = \left[RL_{dq} \right]\left[i_{dq} \right] + \left[L_{dq} \right] p\left[i_{dq} \right] \tag{2.4}$$

where

$$\left[v_{dq}\right]=\left[v_{qs}\ v_{ds}\ v_{qr}\ v_{dr}\right]' \tag{2.5}$$

$$\left[i_{dq}\right]=\left[i_{qs}\ i_{ds}\ i_{qr}\ i_{dr}\right]' \tag{2.6}$$

$$\left[RL_{dq}\right]=\begin{bmatrix} R_s & \omega\left(L_m+L_{ls}\right) & 0 & \omega L_m \\ -\omega\left(L_m+L_{ls}\right) & R_s & -\omega L_m & 0 \\ 0 & \left(\omega-\omega_r\right)L_m & R_r & \left(\omega-\omega_r\right)\left(L_m+L_{lr}\right) \\ -\left(\omega-\omega_r\right)L_m & 0 & -\left(\omega-\omega_r\right)\left(L_m+L_{lr}\right) & R_r \end{bmatrix} \tag{2.7}$$

$$\left[L_{dq}\right]=\begin{bmatrix} L_m+L_{ls} & 0 & L_m & 0 \\ 0 & L_m+L_{ls} & 0 & L_m \\ L_m & 0 & L_m+L_{lr} & 0 \\ 0 & L_m & 0 & L_m+L_{lr} \end{bmatrix} \tag{2.8}$$

Rearranging Equation (2.4)

$$p\left[i_{dq}\right]=\left[L_{dq}\right]^{-1}\left[v_{dq}\right]-\left[L_{dq}\right]^{-1}\left[RL_{dq}\right]\left[i_{dq}\right] \tag{2.9}$$

Since the rotor is squirrel cage, v_{qr} and v_{dr} are both equal to zero. The differential equations representing the capacitor circuit is given by:

$$\begin{bmatrix} i_{cq} \\ i_{cd} \end{bmatrix}=C\begin{bmatrix} p & \omega \\ -\omega & p \end{bmatrix}\cdot\begin{bmatrix} v_{qs} \\ v_{ds} \end{bmatrix} \tag{2.10}$$

where the voltage across the capacitor is v_{qs} and v_{ds} and the currents are i_{cq} and i_{cd}.respectively. Equation (2.10) can be re-arranged to give:

$$p\begin{bmatrix} v_{qs} \\ v_{ds} \end{bmatrix}=\begin{bmatrix} 1/C & 0 \\ 0 & 1/C \end{bmatrix}\begin{bmatrix} i_{qs} \\ i_{ds} \end{bmatrix}+\begin{bmatrix} 0 & -\omega \\ \omega & 0 \end{bmatrix}\begin{bmatrix} v_{qs} \\ v_{ds} \end{bmatrix} \tag{2.11}$$

For open circuit conditions, (2.4) through (2.11) form the set of differential equations to represent the system. For a resistive load connected across the terminals of the SEIG and noting that :

$$i_{qs} = i_{cq} + i_{lq} \tag{2.12}$$

and

$$i_{ds} = i_{cd} + i_{ld}, \tag{2.13}$$

Load currents may be expressed as :

$$R_l \begin{bmatrix} i_{lq} \\ i_{ld} \end{bmatrix} = \begin{bmatrix} v_{qs} \\ v_{ds} \end{bmatrix} \tag{2.14}$$

In order to take the *RL* load impedance into account

$$\begin{bmatrix} v_{qs} \\ v_{ds} \end{bmatrix} = \left(R_l + pL_l\right) \begin{bmatrix} i_{lq} \\ i_{ld} \end{bmatrix} \tag{2.15}$$

or

$$p \begin{bmatrix} i_{lq} \\ i_{ld} \end{bmatrix} = L_l{}^{-1} \begin{bmatrix} v_{qs} \\ v_{ds} \end{bmatrix} - L_l{}^{-1} R \begin{bmatrix} i_{lq} \\ i_{ld} \end{bmatrix} \tag{2.16}$$

2.3 Experimental setup of two industrial 7.5 hp Aluminum- and Copper-rotor SEIGs

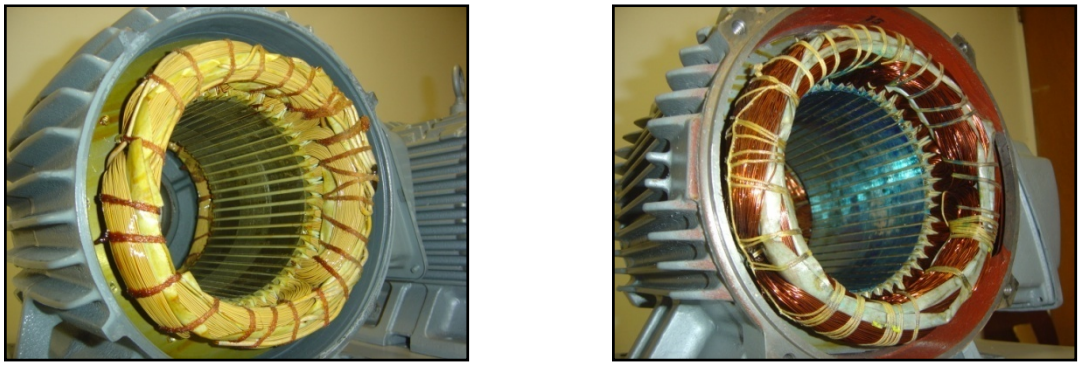

(a) (b)

Fig. 2.31. Stators of the two 7.5 hp induction machines used in the investigations. (a) Aluminum-rotor. (b) Copper-rotor.

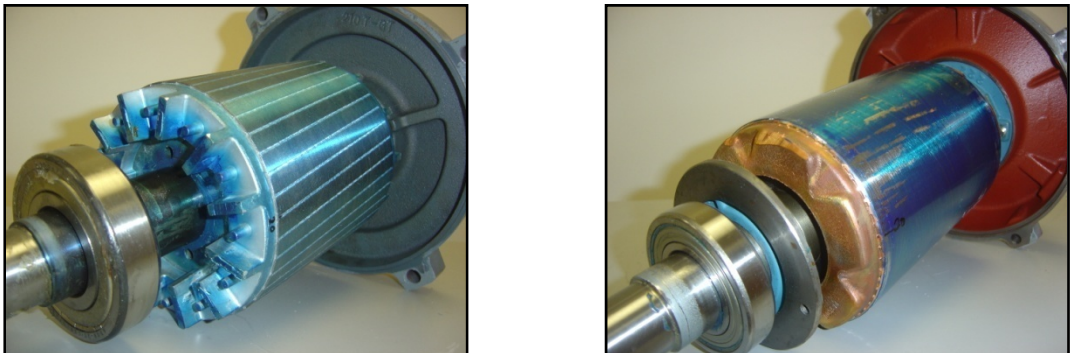

(a) (b)

Fig. 2.32. Rotors of the two 7.5 hp induction machines used in the investigations. (a) Aluminum-rotor. (b) Copper-rotor.

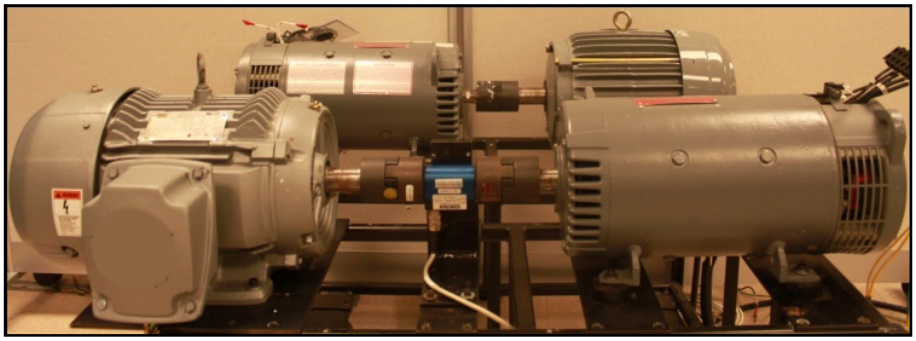

Fig. 2.33. Experimental setup of the DC motor coupled ALSEIG and CRSEIG systems used in the investigations.

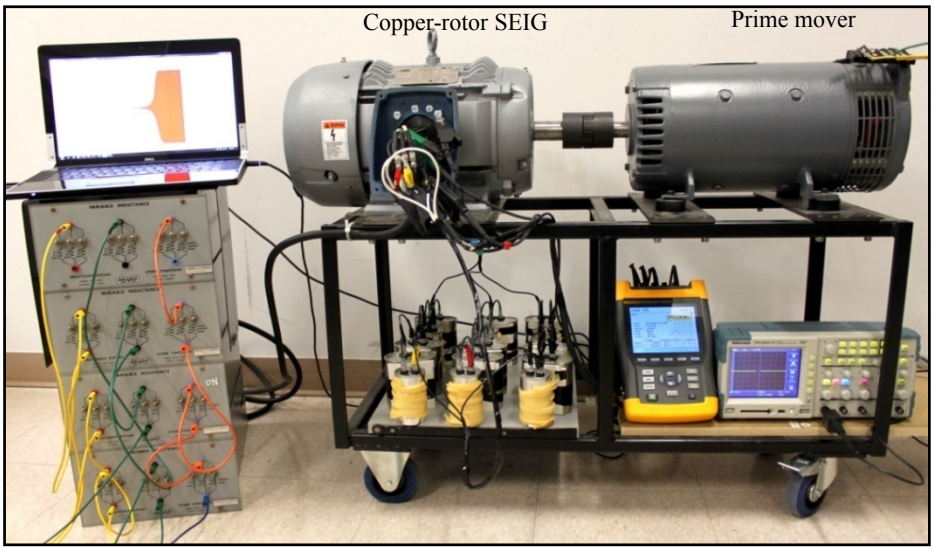

Fig. 2.34. Experimental setup of the DC motor coupled CRSEIG system with the load bank, capacitor bank, Tektronix oscilloscope and Fluke power quality analyser used in the investigations.

TABLE 1
INDUCTION GENERATOR DATA

	Aluminum-rotor SEIG	Copper-rotor SEIG
Output power	7.5 hp	7.5 hp
Rated voltage	346 V	460 V
Rated current	12 A	9.5 A
Connections	Wye	Wye
Number of poles	4	4
Rated speed	1755 rpm	1775 rpm
Rated frequency	60 Hz	60 Hz
Weight	75.9 kg	90 kg
Diameter of rotor	134.9 mm	129.9 mm
Height of rotor bar	25.79 mm	26.6 mm
Width of rotor bar	5.62 mm	5.6 mm
Length of rotor bar	136.8 mm	167.8 mm
Number of conductors	40	40
Conductivity of rotor bar	37.71 μS/mm	59.61 μS/mm
R_s [Ω]	0.38621	0.65417
R_r [Ω]	0.81736	1.48166
X_{ls} [Ω]	0.92557	2.08272
X_{lr} [Ω]	1.38835	3.12267
X_m [Ω]	40.6851	68.9616
R_c [Ω]	564.580	1031.24

2.4 Validating the developed conventional two-axis model of SEIG for both copper- and aluminum-rotor SEIGs

In order to validate the theory and modeling of the two-axis model of SEIGs developed in the previous part of this section, performance of two industrial 7.5 hp aluminum- and copper-rotor SEIGs was elicited through a developed computer program and an experimental set-up. The machine equivalent circuit parameters, resistances and inductances determined from the standard no-load, dc and blocked rotor tests, are presented in Table 1. Output parameters of both the machines were calculated by employing the developed two-axis model and were experimentally verified, for varying power factor loads. The measurements were taken using a Tektronix 2024 digital storage oscilloscope, a Fluke 434 power quality analyser, after the machines reached a speed of 1800 rpm and the experimental setup is as shown in Figs. 2.31 through 2.34 in the previous section. The calculated and measured terminal voltage, reactive power and stator current profiles of both aluminum- and copper-rotor SEIGs are shown in Figs. 2.41

and 2.42. The results shown in Figs. 2.41 and 2.42 were elicited under a static *RL* load applied across the stator terminals at around 62 seconds and 82 seconds for aluminum- and copper-rotor SEIGs respectively, after their voltages had reached steady state. From these figures, it can be observed that there is a minimal variation in the measured and calculated results obtained using the conventional two-axis model of SEIG. This variation in results can be explained as elucidated in [25]-[27]. Results obtained using the developed two-axis model can be improved to match the experimental results by incorporating various AC conduction effects in the rotors of both the machines which is done in the following section.

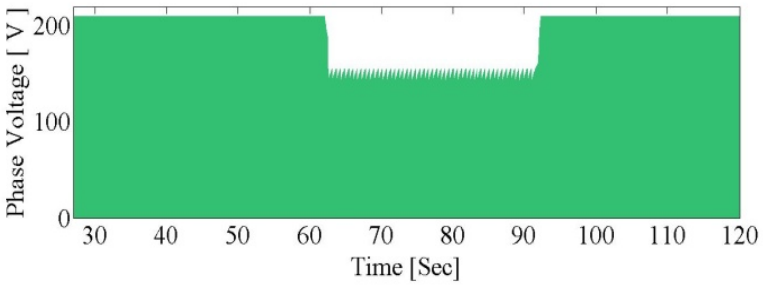

(a)

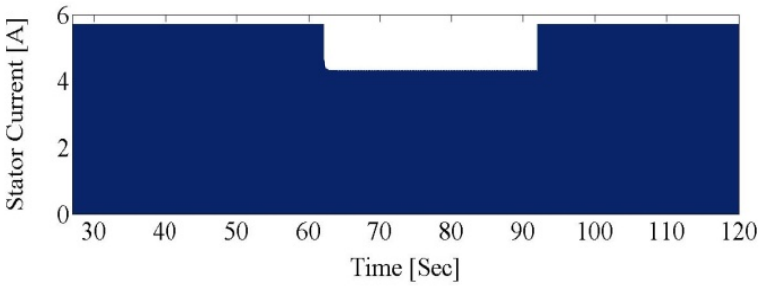

(b)

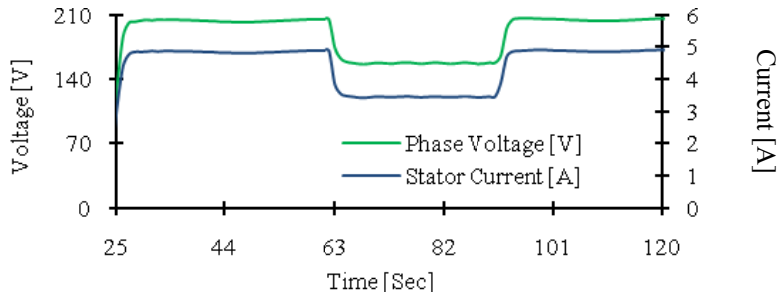

(c)

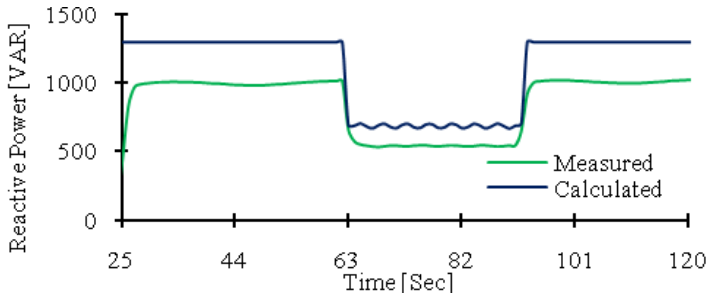

(d)

Fig. 2.41. Calculated and measured positive half cycle results of aluminum-rotor SEIG under *RL* load of 200 Ω and 0.26 H after the machine reached a rated speed of 1 pu at an excitation capacitance of 65 μF. (a) Calculated phase voltage profile. (b) Calculated stator current profile. (c) Measured phase voltage and stator current profiles. (d) Calculated and measured reactive power profiles.

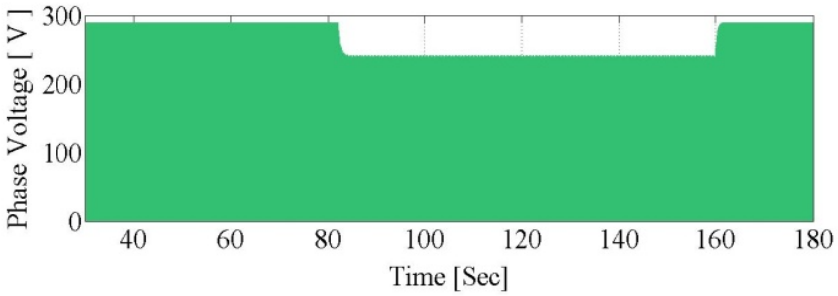

(a)

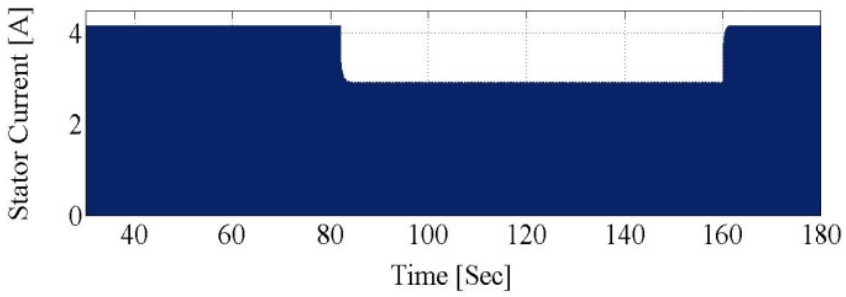

(b)

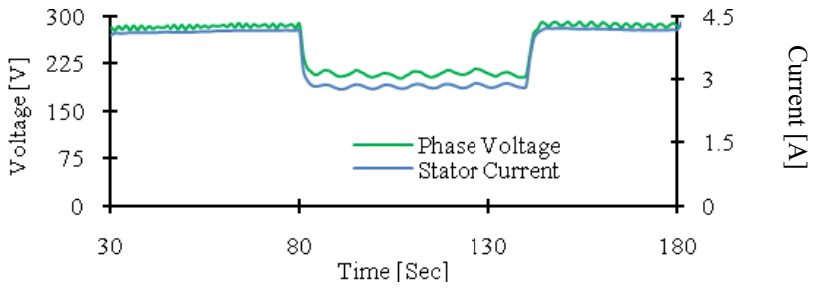

(c)

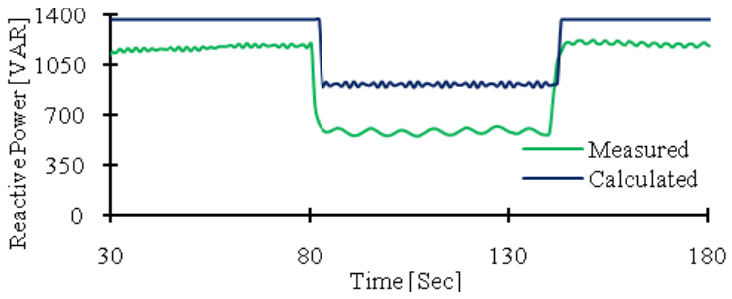

(d)

Fig. 2.42. Calculated and measured positive half cycle results of copper-rotor SEIG under *RL* load of 340 Ω and 0. 44 H after the machine reached a rated speed of 1 pu at an excitation capacitance of 39.6 μF. (a) Calculated phase voltage profile. (b) Calculated stator current profile. (c) Measured phase voltage and stator current profiles. (d) Calculated and measured reactive power profiles.

2.5 Electromagnetic Modeling of Skin and Proximity Effects in the Rotor Bar of the Aluminum- and Copper- Rotor SEIGs used in the investigations

A. Introduction to AC conduction effects

A century ago, Lord Kelvin showed that any rapid change of current intensity in a conductor modifies the current density profile in various parts of the conductor. This reminds us of the consequences of proximity effect in the case of electrical conductors designed for high frequency currents. More attention should be paid to this phenomenon while designing rotor bars for electrical machines since it is clear that this, when neglected, leads to higher energy losses and poor overall operational efficiency [25].

As shown in Figs. 2.51(a) and (b), alternating currents have a preference of moving to the periphery of solid conductors. This tendency of current to concentrate on the surface of the conductor rather than the center itself is due to its high frequency which further increases the inductive reactance at the center of the conductor forcing the electrical charges towards the outer surface. Hence, when the concentration of charges increases at the surface, the charges have very minimal free space for motion and cause heat, energy emission due to friction. This increase in the current density at the periphery of rotor conductors further increases the resistance at the surface of the conductors.

One explanation often put forward for Fig. 2.51(c) is, the inductance at the center of the

conductor is higher than at the periphery due to large current at the center. Further, this leads to larger flux linkages and higher magnetic field at the center and lesser current flows through the maximum magnetic field region. Hence, this current which is a maximum at the surface keeps decreasing as we go into the conductor and the current density falls to 1/e of its original value.

This characteristic would not have been to its disadvantage if it did not lead to extra losses of energy. In solid conductors, due to these losses and heating, the effective AC resistance appears to be higher than the actual DC resistance [25]. This results in two disadvantages:

- Waste of electrical energy through supplementary losses which industrialists recognize as a luxury of losses which is not limited to only financial considerations.
- Waste of raw materials, copper and aluminum, because of the larger amounts of metals badly used as electrical conductors.

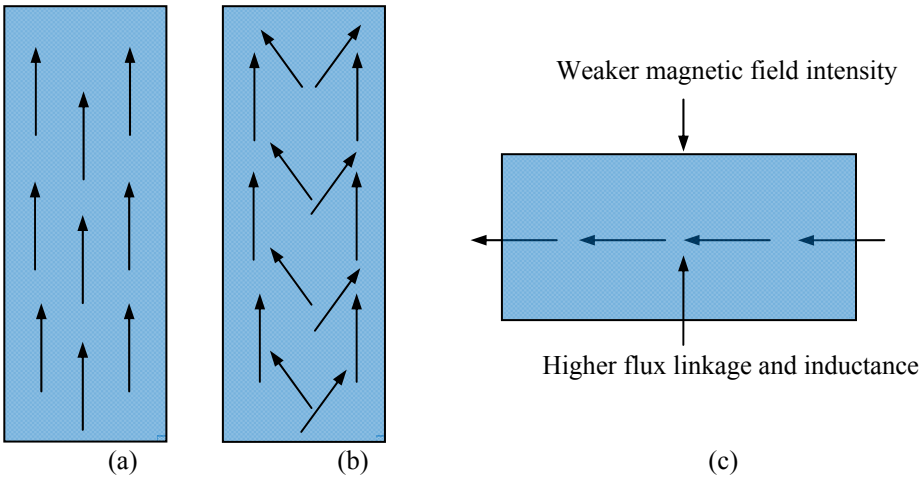

Fig. 2.51. Effects of varying frequency of current in the conductor. (a) Uniform current distribution in ideal case (DC). (b) Heterogeneous current distribution due to skin effect (AC). (c) Effects of varying frequency of current on the inductance and magnetic field intensity.

B. Theory of Proximity effect

In case of a SEIG, the frequency of the current in the rotor is affected by the varying load and speed of the wind turbine. The resulting high frequency of current give rise to a phenomenon called the "Skin Effect" [26]. Skin effect plays an important role in the performance of the SEIG due to the higher current density at the surface of the rotor bars.

Until now, a conductor subjected to skin effect has been considered to be isolated and outside the influence of any magnetic field, except for its own. This assumption is no longer valid when another conductor is in the vicinity; a further distortion in current density occurs due to the interaction of the magnetic field of adjacent conductors. The magnetic flux of one bar induces an e.m.f. in the adjacent conductors, increasing the non uniformity of the current density. If two conductors in close proximity carry currents in opposite directions, their electromagnetic fields are opposed to one another and tend to force the conductors apart. There exists a decrease in flux linkages around the adjacent parts of the conductors and an increase around the outer parts of the same conductor; which results in a concentration of current in the adjacent parts, where the back e.m.f is at a minimum. If the current flows in the same direction, it tends to be concentrated in the remote parts of the conductors. This is known as the "proximity effect" which also increases the resistance of the conductors [28]. Proximity effect can be further classified as direct, inverse and induced proximity effects. In order to elucidate the proximity effect in rotor bars of a SEIG, a case study has been presented below.

C. Case Study

Consider a rectangular conductor as shown in Fig. 2.52 The current density in Fig. 2.52 (a) is higher on the periphery because of the skin effect. Let the conductor be split longitudinally in two halves as shown in Fig. 2.52 (b); no changes yet appear in the current distribution. If these two halves are gradually separated as in Fig. 2.52 (c), the magnetic field of each one changes and the current densities on the surfaces facing each other will increase until they become equal to those of the outside surfaces of the individual conductors. The proximity effect becomes apparent in addition to the skin effect for bars which are electrically and spatially in vicinity to each other and is prominent for a suffciently low separation between the bars of order less than three times their largest dimension [26], [28].

Since the rotor bars can be of copper or aluminum, the performance of these materials under the influence of proximity effect is determined in this paper. Although, copper is a better substitute for aluminum in general, we can increase the efficiency of copper-rotor induction generators if these effects are carefully dealt with. As reported in [27], these effects have been the only concern in further increasing the efficiency of copper-rotor

machines and the higher conductivity of copper allows the rotor designer to use these effects to tailor the behavior of the rotor to improve machine performance.

D. *Modeling the SEIG considering Proximity Effect*

In order to model the proximity effect and later incorporate it into the conventional SEIG model, Maxwell's equations in their integral forms are manipulated into second-order differential equations using the Stokes and Divergence theorems, a frequency domain analysis is then performed by assuming sinusoidal waveforms and setting $d/dt = j\omega$ [29].

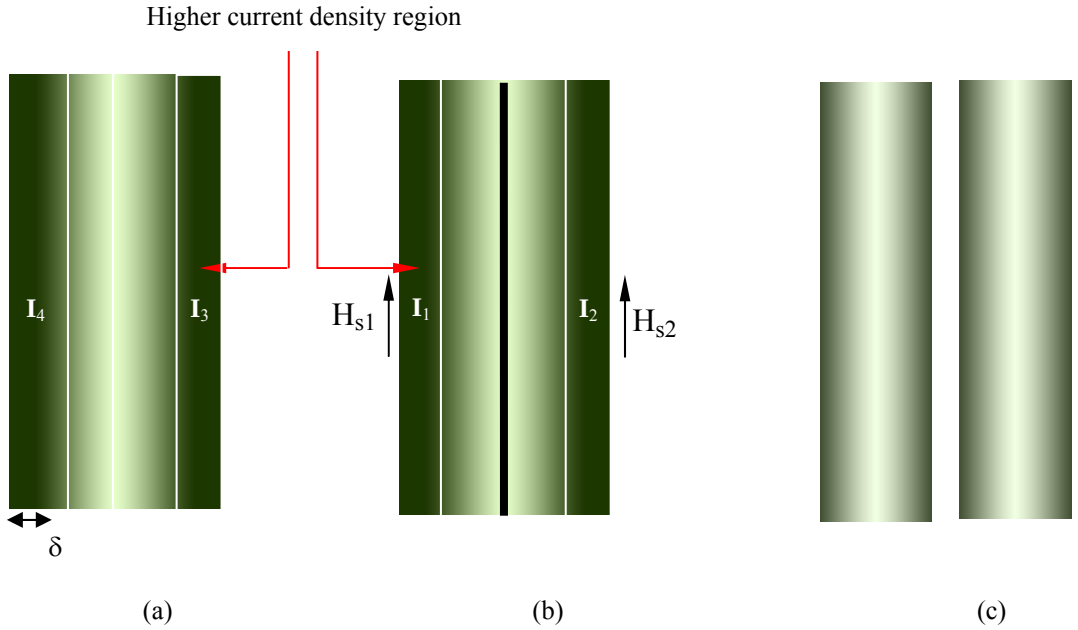

Fig. 2.52. Current distribution. (a) Current density is higher on the periphery due to skin effect. (b) No changes in current distribution, when the conductor is longitudinally bisected. (c) Mutual magnetic fields change the current distribution as the bars are separated. Current density increases on the surfaces facing each other till they become as shown above.

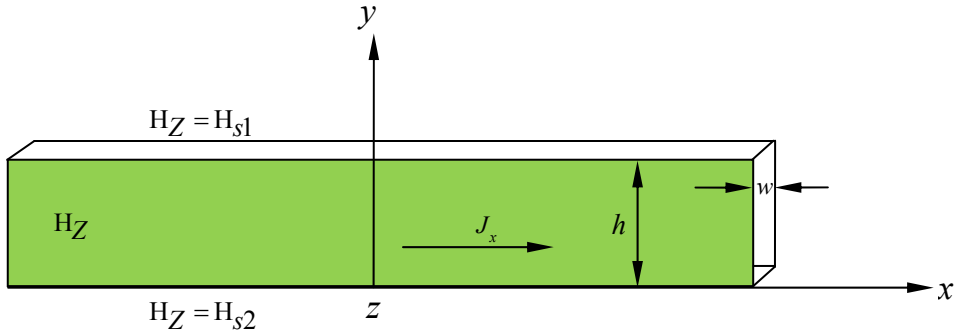

Fig. 2.53. Cross-section of the rectangular rotor bar taken into consideration.

$$\left.\begin{aligned} \nabla \cdot \mathrm{E} &= \rho / \varepsilon \\ \nabla \times \mathrm{E} &= -\mathrm{j}\omega \mathrm{B} \\ \nabla \cdot \mathrm{B} &= 0 \\ \nabla \times \mathrm{B} &= j\omega\varepsilon\mu \mathrm{E} + \mu J \end{aligned}\right\} \tag{2.17}$$

Setting $J = \sigma \mathrm{E}$ and substituting in (2.17),

$$\nabla \times \mathrm{B} = (\sigma + j\omega\varepsilon)\mu \mathrm{E} \tag{2.18}$$

Substitute the second equation of (2.17) in (2.18)

$$\nabla \times \nabla \times \mathrm{E} = -(\sigma + j\omega\varepsilon) j\omega\mu \mathrm{E} \tag{2.19}$$

Insert first equation of (2.17) in the above equation and it becomes:

$$\nabla^2 \mathrm{E} = \frac{\nabla \rho}{\varepsilon} + (\sigma + j\omega\varepsilon) j\omega\mu \mathrm{E} \tag{2.20}$$

Similarly substituting last equation of (2.17) in second equation of (2.17) and rearranging, an expression for B can be obtained:

$$\nabla \times \nabla \times \mathrm{B} = -(\sigma + j\omega\varepsilon) j\omega\mu \mathrm{B} \tag{2.21}$$

Since $\nabla \cdot \mathrm{B} = 0$,

$$\nabla^2 \mathrm{B} = (\sigma + j\omega\varepsilon) j\omega\mu \mathrm{B} \tag{2.22}$$

The term $j\omega\sigma\mu$ is associated with the moving charge and includes the eddy current effect. The other terms can be neglected as they do not contribute in any ways to this modeling of proximity effect [31]-[33]. Recalling (2.20) and (2.22) and taking into account just the required terms:

$$\nabla^2 \mathrm{E} = j\omega\sigma\mu E \tag{2.23a}$$

$$\nabla^2 \mathrm{B} = j\omega\sigma\mu \mathrm{B} \tag{2.23b}$$

Setting $J = \sigma \mathrm{E}$ in (2.23a),

$$\nabla^2 J = j\omega\sigma\mu J \tag{2.24}$$

Since, $\mathrm{B} = \mu_0 \mathrm{H}$ inside the conductors, we can rewrite (2.23b) as:

$$\nabla^2 \mathrm{H} = \alpha^2 \mathrm{H} \tag{2.25}$$

where

$$\alpha = \frac{(1+j)}{\delta} \text{ and } \delta = \frac{1}{\sqrt{\pi f \sigma \mu_0}} = \text{skin depth} \tag{2.26}$$

Equation (2.25) has a solution of the form:

$$\mathrm{H}_Z = K_1 e^{\alpha y} + K_2 e^{-\alpha y} \tag{2.27}$$

Consider the conductor bar to have a height, *h*, and width, *w,* as shown in Fig. 2.53. If the current carried by the conductor is *I*, application of Ampere's circuital law yields the following boundary values:

$$\mathrm{H}_{s1} = -\mathrm{H}_{s2} = I/w \tag{2.28}$$

Solving for H yields:

$$\mathrm{H}_Z = \frac{I \cosh \alpha y}{w \sinh ah/2} \tag{2.29}$$

Since $\frac{d\mathrm{H}_Z}{dy} = J_X$ we get:

$$J_X = \frac{\alpha I \cosh \alpha y}{2w \sinh ah/2} \tag{2.30}$$

The loss per unit length of the conductor is given by:

$$P1s = \frac{I^2}{4w\sigma\delta} \frac{\sinh u + \sin u}{\cosh u - \cos u} \tag{2.31}$$

with $u = h/\delta$

Diffusion equation (2.24) can be simplified to:

$$\frac{d^2 J_X}{dX^2} = \alpha^2 J_X \tag{2.32}$$

where, α is given as in (2.26). The general solution of (2.32) is:

$$J_X = P \cosh \alpha y + Q \sinh \alpha y \tag{2.33}$$

Following (2.28) and considering:

$$\mathrm{H}_{s1} = \frac{(k-1)I}{w} \tag{2.34}$$

$$\mathrm{H}_{s2} = \frac{kI}{w} \tag{2.35}$$

where, k is any real number [30]. The magnetic field intensity inside the conductor is given as:

$$\mathrm{H}_Z(y) = \frac{1}{w}\left[I(k-1) + \int_0^y w J_X \, dy \right] \tag{2.36}$$

The magnetic flux density is:

$$\mathrm{B}_Z(y) = \mu_0 \left[\frac{I(k-1)}{w} + \int_0^y J_X \, dy \right] \tag{2.37}$$

The electric field along the length is composed of an inductive and resistive voltage drop;

$$\mathrm{E}_X = \rho J_X + j\omega(\varphi_l + \varphi_e) \tag{2.38}$$

Where, φ_l and φ_e are the internal and external flux linkages respectively. Equation (2.38) can be simplified by differentiating it with respect to y and utilizing the fact that E_x is constant over the height of the conductors [33].

$$0 = \frac{d\mathrm{E}_X}{dy} = \rho \frac{dJ_X}{dy} + j\omega d(\varphi_l + \varphi_e) \Big/ dy \tag{2.39}$$

Since φ_e is constant and $\frac{d\varphi_l}{dy} = \mathrm{B}_Z$, we get:

$$\frac{dJ_X}{dy} = -j\omega\sigma \mathrm{B}_Z \tag{2.40}$$

Substituting (2.40) in (2.37)

$$\frac{dJ_X}{dy} = j\omega\mu_0\sigma \left[\frac{I(k-1)}{w} + \int_0^y J_X \, dy \right] \tag{2.41}$$

Setting y=0 in (2.41), we get:

$$Q = \frac{\alpha I(k-1)}{w} \tag{2.42}$$

The total current is simply the integral of the current density:

$$I = w\int_0^h J_X dx \tag{2.43}$$

and we obtain:

$$P = \frac{I\alpha}{w}\left[\frac{1}{\sinh \alpha h} + (1-k)\tan \alpha h/2\right] \tag{2.44}$$

Considering at the top ($y=h$), equation (2.39) then becomes:

$$J_X = \frac{I\alpha}{w}\left[\frac{\cosh \alpha x}{\sinh \alpha h} - (k-1)\tan \alpha h/2 + (k-1)\sinh \alpha x\right] \tag{2.45}$$

The voltage drop per unit length on the surface of the conductor is:

$$E_X = \frac{J_{X\,top}}{\sigma} \tag{2.46}$$

Divide both sides of (2.46) by I, we obtain the resistance coefficient K_r and inductance coefficient K_l due to the influence of skin effect can be written as:

$$\left.\begin{aligned} K_r &= \frac{1}{\sigma w \delta}\left[\frac{\sinh 2u + \sin 2u}{\cosh 2u - \cos 2u} + (k-1)\frac{\sinh u - \sin u}{\cosh u + \cos u}\right] \\ K_l &= \frac{1}{2\pi f \sigma w \delta}\left[\frac{\sinh 2u - \sin 2u}{\cosh 2u - \cos 2u} + (k-1)\frac{\sinh u + \sin u}{\cosh u + \cos u}\right] \end{aligned}\right\} \tag{2.47}$$

$$R_{r\_skin} = R_{r0} \times K_r \tag{2.48}$$

$$L_{lr\_skin} = L_{lr0} \times K_l \tag{2.49}$$

Multiplying the coefficients K_r and K_l in (2.47) with the original resistance R_{r0} and inductance L_{lr0} respectively of the machine, we obtain the new resistance R_{r_skin} and inductance L_{lr_skin} as a function of skin effect, as shown in (2.48) and (2.49) respectively [26].

$$\left.\begin{aligned} \mathrm{H}_{s1} &= -\mathrm{H}_{s2} = I/w \\ k' &= \frac{1}{\left(1+\frac{\mathrm{H}_{s1}}{\mathrm{H}_{s2}}\right)} \end{aligned}\right\} \tag{2.50}$$

C_{r_prox} and C_{l_prox} are later multiplied by the skin effect resistance and inductance, R_{r_skin} and L_{lr_skin}, in order to allow an influence of the proximity effect. Hence, the effective rotor resistance R_{r_eff} and inductance L_{lr_eff} as in (2.51) are obtained as a function of the proximity effect and used in the conventional machine model.

Proximity effect multiplication factors C_{r_prox} and C_{l_prox} are calculated from the ratios of K_r and K_l, correspondingly, at k=1/2 and k=k' from (2.47). The value of k' is calculated through an iterative solution of equations involving rotor current as in (2.50). The influence of current redistribution is incorporated by utilizing uniform current distributions in an area of δ, as indicated in Fig. 2.32. Also, it is assumed that the values of the currents in the regions 1, 2, 3 and 4 shown in Fig. 2.32 are I_1=-I_4 and I_2=-I_3, respectively [30].

$$\left.\begin{aligned} R_{r\_eff} &= C_{r\_prox} \times R_{r\_skin} \\ L_{lr\_eff} &= C_{lr\_prox} \times L_{lr\_skin} \end{aligned}\right\} \tag{2.51}$$

2.6 Saturation characteristics of the 7.5hp Aluminum and Copper-rotor induction machines considered in this thesis

It is well known that the voltage build up of an isolated Self Excited Induction Generator is attained through a transient process that reaches equilibrium due to saturation of the magnetic material of the machine. At the state of equilibrium, or steady state operating condition, the magnetizing reactance of the machine must be equal to the slope of the reactance of the excitation capacitor. The evaluation of the saturation level and the mutual inductance term at a particular operating condition require the accurate representation of the magnetization curve of the induction machine under consideration. In order to model an SEIG accurately, the variation of the magnetizing inductance with

current needs to be determined as the magnetizing inductance is the key element for voltage build-up and stability. In this research the saturation curve has been measured with the machine driven at synchronous speed by a shunt connected dc motor. A three phase balanced voltage is applied to the stator terminals. The voltage is gradually varied from 0 to about 120% of rated voltage and the corresponding current at each step is recorded. The saturation curves with the phase voltage as a function of current and at rated frequency is shown in Fig. 2.61. It can be seen that the value of the magnetizing inductance increases in the linear region of the magnetizing characteristics but decreases with the increase of magnetizing current owing to magnetic saturation. The magnetizing inductance can be represented by piecewise linearization or by other mathematical functions [34].

In order to take the effect of magnetic saturation of the machines into account, the saturation characteristics of the induction generator is determined from standard laboratory tests as shown above. The nonlinear relationship between the magnetizing inductance X_m and the magnetizing current i_m in actual quantities for the aluminium rotor and the copper rotor SEIGs are derived from its respective magnetizing characteristics and given in Fig 2.62 and Fig. 2.63, respectively. The nonlinear nature of the relationship can be expressed in several ways. Some authors have proposed piece-wise linearization [35][36], or by using higher order polynomials [37],[38] or a continuous function [39]-[41].

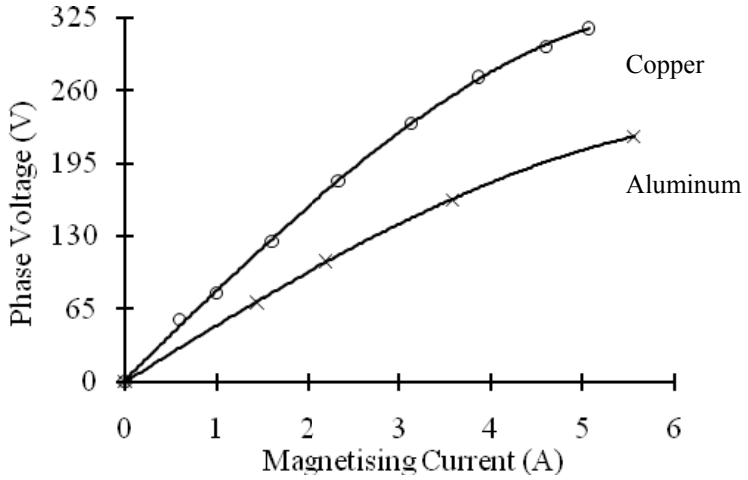

Fig. 2.61 Measured saturation characteristics of both aluminum- and copper-rotor machines taken into consideration.

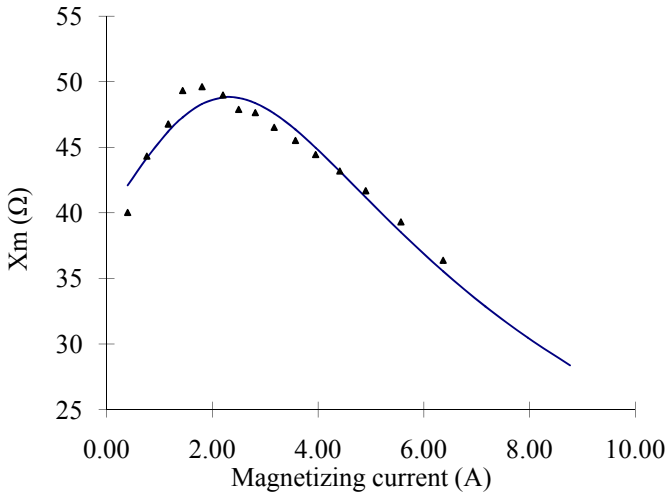

Fig. 2.62 Magnetizing inductance of 7.5 hp aluminum rotor SEIG used in the investigation.

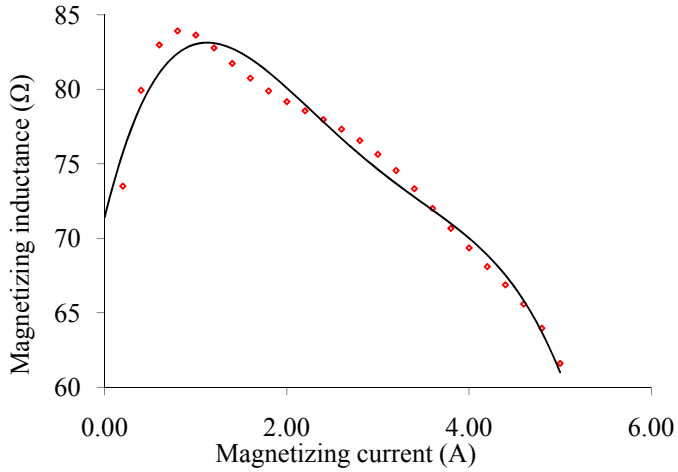

Fig. 2.63. Magnetizing inductance of 7.5 hp copper rotor SEIG used in the investigation.

Saturation characteristics of both aluminum- and copper-rotor machines are incorporated in the above two axis model using an arctangent continuous function to replace a curve fitting polynomial method in order to obtain better accuracy in the investigations [42].

$$X_m = \alpha\left(\arctan\left(\beta * i_m - \gamma\right) + \delta\right) / i_m \tag{2.52}$$

where, the coefficients α, β, γ and δ are determined from nonlinear least squares or nonlinear least-squares regression method using Matlab program. At each integration step of the program, the magnetizing current is calculated from the relation:

$$i_m = \sqrt{\left(i_{qs} + i_{qr}\right)^2 + \left(i_{ds} + i_{dr}\right)^2} \tag{2.53}$$

From the calculated value of i_m the value of X_m is derived from Equation (2.53) and updated at each integration stage in the main Matlab routine.

The phase voltages and currents are calculated using the inverse of the classical transformation matrix T, where

$$T = \frac{2}{3}\begin{bmatrix} \cos(\omega t) & \cos(\omega t - \frac{2\pi}{3}) & \cos(\omega t + \frac{2\pi}{3}) \\ \sin(\omega t) & \sin(\omega t - \frac{2\pi}{3}) & \sin(\omega t + \frac{2\pi}{3}) \\ \frac{1}{2} & \frac{1}{2} & \frac{1}{2} \end{bmatrix} \tag{2.54}$$

and ω is the speed of the rotating reference frame in the d-q axes.

2.7 Validating the developed Proximity Effect model for two industrial 7.5 hp Aluminum- and Copper-rotor SEIGs

In order to validate the proximity effect model elucidated in section 2.5**,** performance of two industrial 7.5 hp aluminum- and copper-rotor SEIGs was elicited through a developed computer program and an experimental set-up. The machine equivalent circuit parameters, resistances and inductances were determined from the standard no-load, dc and blocked rotor tests. The machine equivalent circuit parameters, resistances and inductances determined from the standard no-load, dc and blocked rotor tests, for both the machines are presented in Table 1. Output parameters of both the machines were calculated by employing the conventional two-axis model and the proposed SEIG model with proximity effect and were experimentally verified, for varying power factor loads. The measurements were taken using a Tektronix 2024 digital storage oscilloscope, a Fluke 434 power quality analyzer, after the machines reached a speed of 1800 rpm.

A. Static Load Condition

The analysis on calculated and measured real and reactive power profiles shown in Figs. 2.71 and 2.72 for both the machines explain that the real and reactive power profiles

obtained using the conventional two-axis model of SEIG does not match with the experimental results, whereas, the real and reactive power profiles obtained from the developed proximity effect model and experimental results are in closer agreement, in case of both the machines. This immediacy in results can be attributed to the changing resistance and inductance due to the proximity effect in the rotor bars of the machines.

The varying rotor resistance and inductance due to varying frequency and current distribution in the rotor bars are used to calculate the effective current in the rotor bar and hence, the stator current of the machine. This stator current is later used to calculate the terminal voltage of the machine. Hence, the inaccuracy of the conventional two-axis model which does not incorporate proximity effect is accounted for.

The behavior of real and reactive power was observed at the machine terminals after loading the machines with a *RL* load through numerical and experimental investigations. A load resistance of 100 Ω and inductance of 0.44 H was applied to the aluminum-rotor machine at 15 seconds and calculated reactive and real power profiles are illustrated in Figs. 2.71(a) and (b).

The results calculated using the proximity effect model are closer to the measured ones as shown in Figs. 2.71(c) and (d), when compared with that of the conventional two-axis model. The real and reactive power obtained using the developed model are lesser than that of conventional model and closer to the measured results, as the developed model incorporates proximity effect losses in the rotor bars.

Similarly, the copper-rotor machine was loaded at 20 seconds with a load resistance of 280 Ω and inductance of 0.22 H and the corresponding results obtained on calculations and measurements are as shown in Fig. 2.72. Similar to the results of aluminum-rotor machine, the calculated results using the proximity effect model are closer to that of the experiments for the copper-rotor machine as well. It is also observed that the real and reactive power calculated through both the models have a comparatively higher variation than that of the aluminum-rotor machine due to the higher proximity effect power loss in copper-rotor machine.

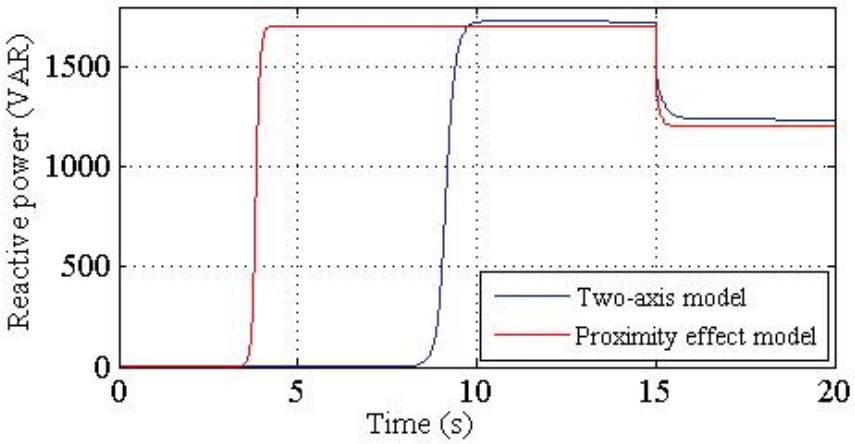
Reactive power (VAR)
1500
1000
500
0
0
5
10
15
20
Time (s)
Two-axis model
Proximity effect model

(a)

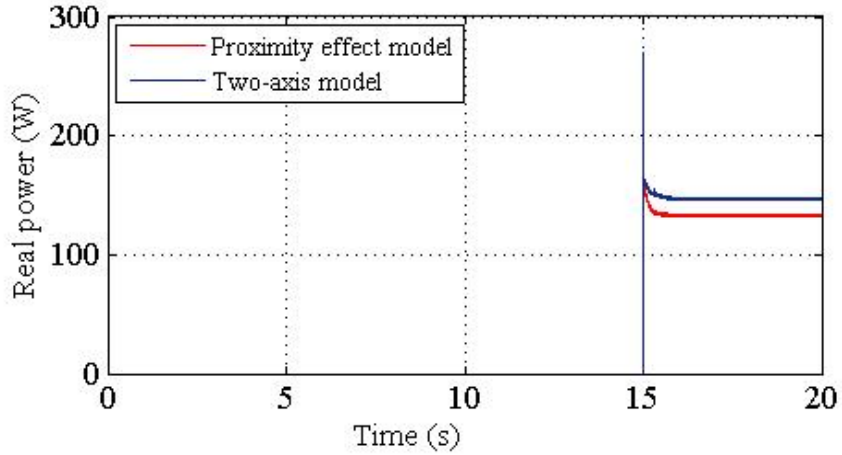
Real power (W)
300
200
100
0
0
5
10
15
20
Time (s)
Proximity effect model
Two-axis model

(b)

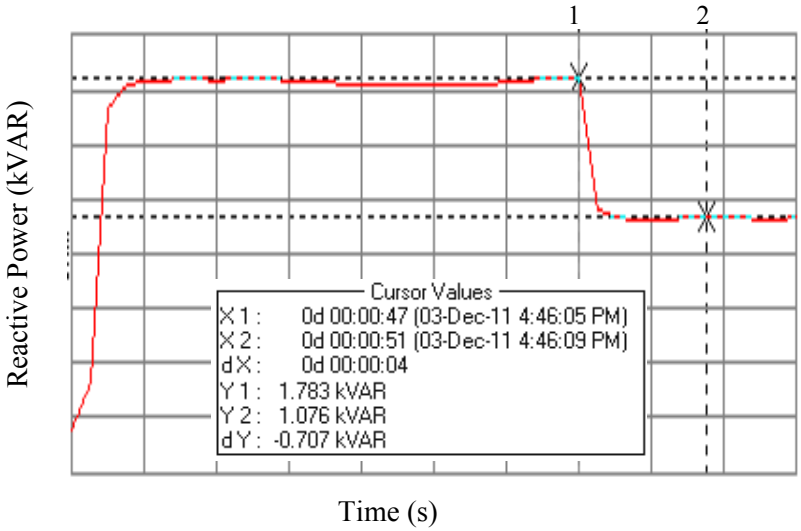
1
2
Reactive Power (kVAR)
Cursor Values
X 1 : 0d 00:00:47 (03-Dec-11 4:46:05 PM)
X 2 : 0d 00:00:51 (03-Dec-11 4:46:09 PM)
dX : 0d 00:00:04
Y 1 : 1.783 kVAR
Y 2 : 1.076 kVAR
dY : -0.707 kVAR
Time (s)

(c)

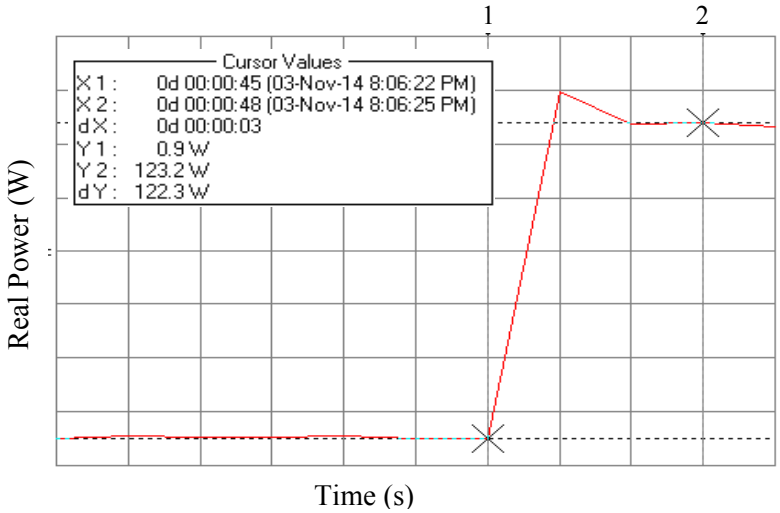

(d)

Fig. 2.71. Calculated and measured reactive and real power profiles under RL load for aluminum-rotor SEIG at a rotor speed of 1 pu. (a) Calculated reactive power. (b) Calculated real power. (c) Measured reactive power. (d) Measured real power.

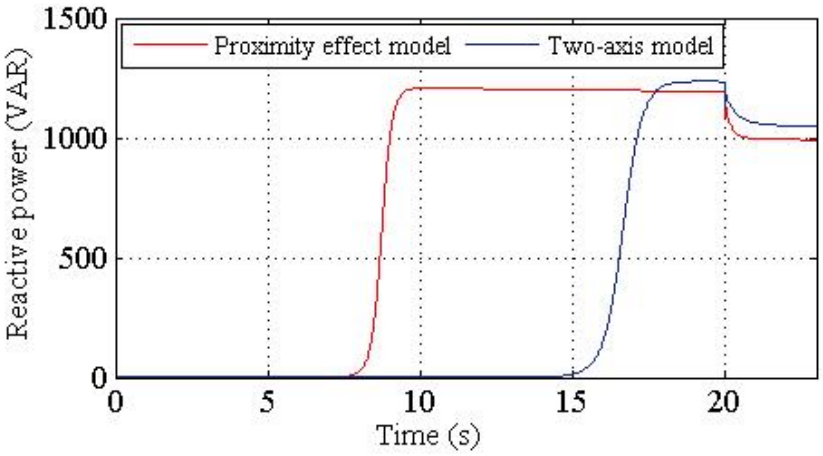

(a)

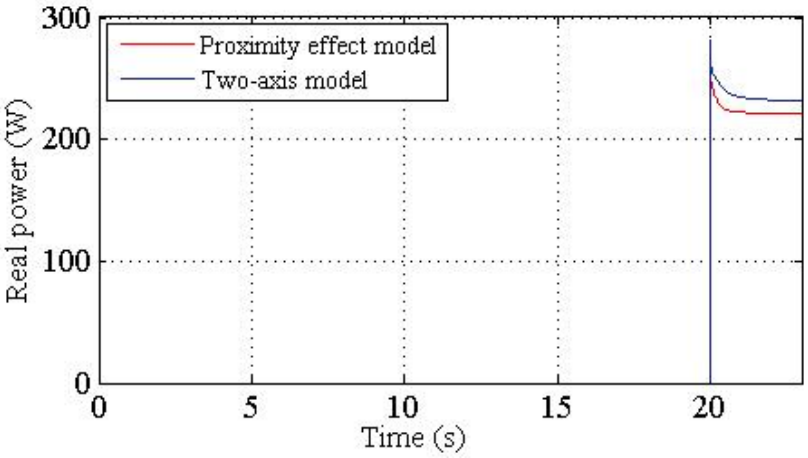

(b)

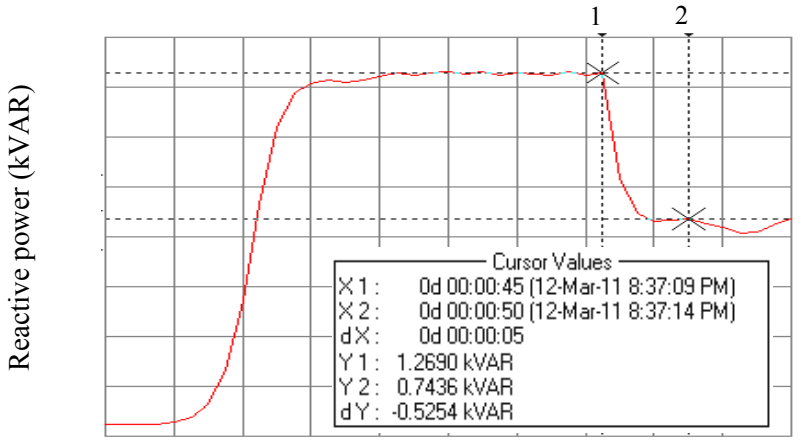

(c)

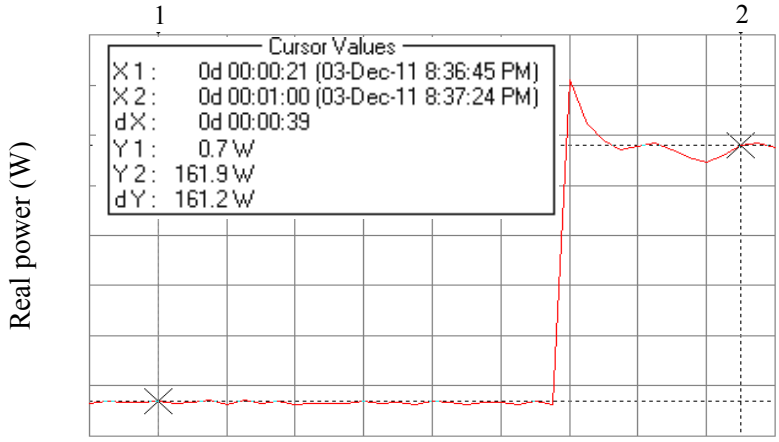

(d)

Fig. 2.72. Calculated and measured reactive and real power profiles under RL load for copper-rotor SEIG at a rotor speed of 1 pu. (a) Calculated reactive power. (b) Calculated real power. (c) Measured reactive power. (d) Measured real power.

B. Power Loss due to Proximity Effect at Varying Frequencies of Rotor Current

Figures 2.73(a) and 2.73(b) show the calculated proximity effect losses in the rotor bars of the aluminum- and copper-rotor machines, respectively. These figures support the theory of proximity effect which states that an increase in the rotor resistance as a function of frequency leads to increased power loss.

For the machines under study, the loading is varied from no-load condition to full load condition and all the machine parameters are measured. The measured values of stator currents are used to calculate the corresponding values of rotor current. Also, the developed mathematical model is used to calculate the rotor current. These values of rotor currents are in close agreement. The losses after incorporating proximity effect are calculated using the analytical model developed for estimation of increased resistance of conductors due to proximity effect. Similarly, using the same analytical model, losses are estimated for a range of currents observed from no-load to full load.

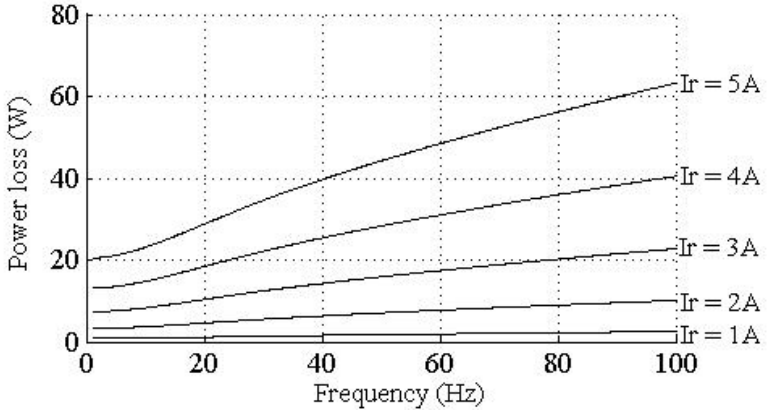

(a)

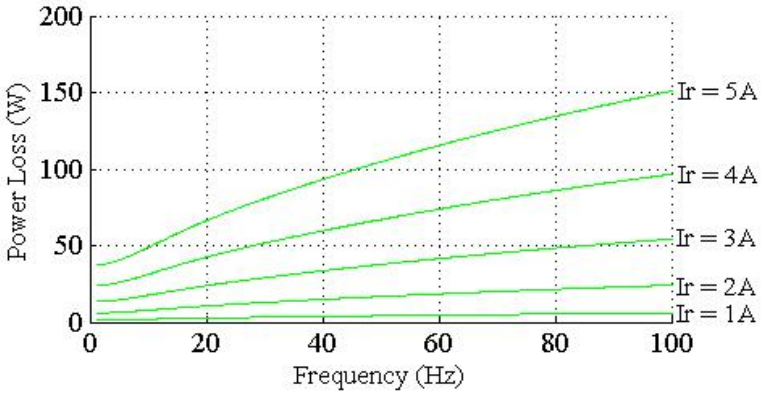

(b)

Fig. 2.73. Power loss due to proximity effect as a function of frequency of rotor current. (a) Aluminum-rotor machine. (b) Copper-rotor machine.

2.8 References

[1] C. Grantham, D. Sutanto, B. Mismail, "Steady-State and Transient Analysis of Self Excited Induction Generators," *IEE Proceedings on Electric Power Applications*, Vol. 136, Pt. E, No. 2, pp. 61-68, Mar. 1989.

[2] Vlado Ostović, *Computer-aided analysis of electric machines : a Mathematica approach*, Hemel Hempstead, Herts, Prentice Hall International (UK), England 1994.

[3] R.C. Bansal, "Three Phase Self-Excited Induction Generators: An Overview," *IEEE Transaction on Energy Conversion*, Vol. 20, No. 2, pp. 292-299, Jun. 2005.

[4] O. Ojo, "Minimum Air Gap Flux Linkage requirement for Self Excitation in Stand Alone Induction Generator, "*IEEE Transaction on Energy Conversion*," Vol. 10, No. 3, pp. 484-491, Sep. 1995.

[5] E. Levi, "Applications of Current State-Space Model in Analyses of Saturated Induction Machines," *Electric Power Systems Research* , pp. 203–216, 1994.

[6] A. Kishore, R.C. Prashad and B.M. Karan, "Matlab Simulink Based DQ Modeling and Dynamic Characteristics of Three Phase Self Excited Induction Generator," *Progress in Electromagnetics Research Symposium 2006*, pp. 312-316, Mar. 2006.

[7] C.F. Wagner, "Self-Excitation of Induction Motors with Series Capacitors," *AIEE Transactions*, Vol. 60, pp. 1241-1247, 1941.

[8] S. J. Chapman, *Electrical Machinery Fundamentals*, 2nd ed. McGraw-Hill, New York, 1998.

[9] E. Levi and Y.W. Liao, "An Experimental Investigation of Self-excitation in Capacitor Excited Induction Generators," *Electrical Power Research*, pp. 59-65, 2000.

[10] D. Seyoum, "The Dynamic Analysis and Control of a Self-Excited Induction Generator driven by a Wind Turbine," Ph. D. Dissertation, The University of New South Wales, Australia, 1999.

[11] S.S Murthy, "A Novel Self-Excited Self-Regulated Single Phase Induction Generator. Part-I: Basic System and Theory," *IEEE Transactions on Energy Conversion*, Vol. 8, No. 3, pp. 377-382, Sep. 1993.

[12] N.H. Malik and A.H. Al-Bahrani, "Influence of the Terminal Capacitor on the Performance Characteristics of a Self Excited Induction Generator," IEE Proceedings, Vol. 137, Pt. C, No. 2, pp. 168-173, Mar.1990.

[13] L. Wang and J.Y. Su, "Determination of Minimum and Maximum Capacitance of an Isolated SEIG using Eigenvalue Sensitivity Approach," *Proceedings of International Conference on Power System Technology*, Vol. 1 pp. 610-614, Aug. 1998.

[14] N.H. Malik and S.E. Haque, "Steady State Analysis and Performance of an Isolated Self Excited Induction Generator," IEEE Transaction on Energy Conversion, pp. 134-139, Sept. 1986.

[15] N.H. Malik and A.H. Al-Bahrani, "Influence of the Terminal Capacitor on the Performance characteristic of a Self Excited Induction Generator," IEE Proceedings Vol. 137, Pt. C, No. 2, pp. 168-173, Mar. 1990.

[16] N.H. Malik and A.A. Mazi, "Capacitance Requirements of Self Excited Induction Generators," IEEE Transaction on Energy Conversion, Vol. EC-2, No. 1, pp. 62-69, Mar. 1986

[17] T.F. Chan, "Analysis of Self Excited Induction Generators using Iterative Method," IEEE Transaction on Energy Conversion, Vol. 10, No. 3, pp. 502-507, Sep.1995

[18] —, "Capacitance requirements of Self-Excited Induction Generators," IEEE Transactions on Energy Conversion, Vol. 8, No. 2, pp. 304-311, Jun. 1993.

[19] A.M. Eltamaly, "New Formula to Determine Minimum Capacitance required for Self Excited Induction Generator," IEEE 33rd Power Electronics Specialists Conference, Vol. 1, pp. 106-110, Jun. 2002.

[20] N.H. Malik and AA. Mazi, "Capacitance requirements for Isolated Self Excited Induction Generators", IEEE Transaction on Energy Conversion, Vol. EC-2, No. 1, pp. 62-68, Mar. 1987.

[21] P.C. Krause and C.H. Thomas, "Simulation of symmetrical Induction Machinery," IEEE Transaction on Power Apparatus and Systems, Vol. PAS-84, No. 11, pp. 1038-1044. Nov.

[22] D. Seyoum, "The Dynamic Analysis and Control of a Self-Excited Induction Generator driven by a Wind Turbine," Ph. D. Dissertation, The University of New South Wales, Australia, 1999.

[23] P.C. Krause, Analysis of Electric Machinery and Drive Systems, 2nd Edition, IEEE Press, 2002.

[24] G. Scutaru and C Apostoaia, " Matlab-Simulink Model of a Stand-Alone Induction Generator," pp. 1-8.

[25] A. Ducluzaux, Schneider Electric-Cahier Technique no. 83, "Extra losses in high current conductors by skin and proximity effects," 1983.

[26] K. Hafiz, G. Nanda, and N. C. Kar, "Performance analysis of aluminum and copper rotor induction generators considering skin and thermal effects," IEEE Trans. on Industrial Electronics, vol. 57, January 2010.

[27] Canadian Copper and Brass Development Association, "Technology transfer report - The die cast copper rotor motor," April 4, 2004.

[28] J. D. Milburn, "Skin and proximity effects in heavy-current conductors" in Proc. Student's Quarterly Journal, March 1969, pp. 172-180.

[29] A. Shadowitz, The Electromagnetic Field, Dover Publications: New York, 1975, pp. 2-47, 382-421.

[30] J. A. Ferreira, Electromagnetic Modeling of Power Electronic Converters, Kluwer Academic Publishers: London, 1989, pp.49-75.

[31] K. J. Bins, P. J. Lawrenson, and C. W. Trowbridge, The Analytical and Numerical Solution of Electric and Magnetic Field, John Wiley & Sons : UK, 1992, pp. 69-112.

[32] J. Lammeraner and M. Stafl, Eddy Currents, CRC Press: USA, 1966, pp. 15-38.

[33] R. L. Stoll, The Analysis of Eddy Currents, Clarendon Press: Oxford, 1974, pp. 10-26.

[34] T.F. Chan, "Capacitance Requirements of Self-Excited Induction Generators," IEEE Transactions on Energy Conversion, Vol. 8, No. 2, pp 304-311, June 1993.

[35] A.K. Tandon, S.S. Murthy and G.J. Berg, "Steady State Analusis of Capacitor Self-Excited Induction Generators," IEEE Transactions on Power Apparatus and Systems, Vol. PAS-103, No, 3 pp. 612-617, Mar. 1984.

[36] L. Wang and C.H. Lee, "A Novel Analysis on the Performance of an Isolated Self-Excited Induction Generator," IEEE Transactions on Energy Conversion, Vol. 12, No. 2, pp. 109-117, Jun. 1997.

[37] L. Wang and C.M. Cheng, "Selection of Magnetizing Curves for Accurately Simulating a Three-Phase Self-Excited Induction Generator Feeding a Single-Phase Load," IEEE Power Engineering Society Winter Meeting, Vol. 1, No. 1, pp. 286-290, 2000

[38] D. Seyoum, C. Grantham and F. Rahman, "A Novel Analysis of an Isolated Self-Excited Induction Generator Taking Iron Loss into Account," IEEE Transaction on Industrial Applicationa, Vol. 35, No. 3, Apr. 2003.

[39] S.S. Kou and L. Wang, "Dynamic Eigenvalue Analysis of a Self-Excited Induction Generator Feeding an Induction Motor," IEEE Power Engineering Society Winter Meeting, Vol. 3, No. 1, pp. 1393-1397, 2001

[40] —, Steady-State Performance of a Self-Excited Induction Generator Feeding an Induction Motor," Electric Power Components and Systems, Taylor and Francis, pp. 581-593, 2002

[41] O. Ojo, "Minimum Air Gap Flux Linkage Requirement for Self-Excitation in Stand Alone Induction Generators," IEEE Transaction on Energy Conversion, Vol. 10, No. 3, pp. 484–492, Sept. 1995

[42] S. C. Kuo, and L. Wang, "Steady-state performance and dynamic stability of a self excited induction generator feeding an induction motor," in Proc. 2000 IEEE International Conference on Electric Machines, vol. 2, pp. 1143-1147.

3.0 STUDY OF COMMERCIALLY AVAILABLE COPPER- AND ALUMINUM-ROTOR INDUCTION MOTORS FOR DISTRIBUTED WIND POWER GENERATION

3.1 Introduction

A commercially available induction motor to the general consumer can be used as a SEIG. It is readily available to the consumer for any application (motoring/ generating). Buying a generator directly might be expensive as low rating generators for small wind farms are not mass produced. However, the performance of these motors as SEIGs can be only judged based on their voltage regulation, frequency regulation and VAR requirement characteristics at different operating conditions. Recently, due to the growing cost and complexity of voltage regulating schemes the need has been felt to develop an economical regulating scheme and also minimally modify the induction motor to improve its generating characteristics and reduce its dependency on regulating schemes.

However, conventional induction motors can be efficiently used as SEIGs if they are either minimally redesigned for the same application or by choosing the best out of the available induction machines through suitability analysis. This chapter exclusively studies the suitability of the relatively newer copper-rotor induction motor (CRIM) and the conventional aluminum-rotor induction motor (ARIM) for use as a SEIG in DWPG. Experimental investigations are performed on two 7.5 hp CRIM and ARIM and the measured results are corroborated by discussions.

3.2 Experimental investigation of CRIM and ARIM to be used as SEIGs in Distributed Wind Power Generation

As discussed in the previous chapter 2, self-excitation in an induction machine can be initiated by connecting a suitable capacitor bank across the machine's terminals. The value of the terminal voltage of the generator depends on the value of capacitor, speed, load and saturation of the magnetic circuit. Besides, the induction motor operating as a SEIG will have poorer efficiency due to higher losses in the rotor which is actually designed to obtain good starting performance in the motor. However, an induction motor with lower winding resistance and leakage reactance should have a better performance in

terms of efficiency and power factor when operated as a SEIG [22].

Experimental investigations were performed on two commercially available 7.5 hp copper- and aluminum-rotor induction motors used as SEIGs (hereafter to be referred as copper-rotor SEIG/ CRSEIG and aluminum-rotor SEIG/ ALSEIG, respectively). The measurements were taken using a Tektronix 2024 digital storage oscilloscope, a Fluke 434 power quality analyzer.

This analysis is performed at the constant rated voltage of the machines at a constant rotor speed of 1 pu as it is desired that the generator provides a constant terminal voltage under varying loads in the field application. This would also enable us to find amount of capacitance required by the machine to maintain the terminal voltage under varying loads. Stepped capacitor switching has been used to keep the terminal voltage constant. Also, the rated stator current of these machines is taken to be the constraint for maximum power delivery as the temperature rise in the stator windings have to be taken into account and kept under permissible limits when determining the maximum permissible loading of the machines. It is also seen from the investigations shown in Fig. 3.21 that the magnitude of the rotor current is lesser than the stator current, hence taking the stator current of the machines to be a constraint is wise as the rotor is competent than the stator to withstand thermal overloads, if any.

The output power of both the machines were measured keeping a constant rated voltage of the respective machines at the machine terminals by using mechanically-switched capacitor banks, in coarse and fine resolutions, available at the laboratory. Figs. 3.21(a) and (b) show the maximum output power that can be delivered by both CRSEIG and ALSEIG without exceeding their rated current. The CRSEIG could be loaded more than the ALSEIG because of its lower losses, better power factor and hence, has been found to yield higher efficiency. The CRSEIG operates at a slip of 1.05% and the ALSEIG operates at a slip of 1.82% at their maximum loading conditions, which is lower than the rated slip of the respective machines. In order to compare the performance of the generators, a factor K may be defined as the ratio of maximum power that can be extracted from the generator keeping the stator current limit, to the rated power of the motor.

$$K = \frac{\sqrt{3} V_{Line} I_{load} Cos\Phi_{load}}{P_m} \tag{3.1}$$

where, P_m is the rated power of the motor.

The K for CRSEIG and ALSEIG is found to be 1.204 pu and 1.126 pu, respectively. Previous research performed did not consider the capacitor excitation currents while calculating the additional power delivering capacity of the machines.

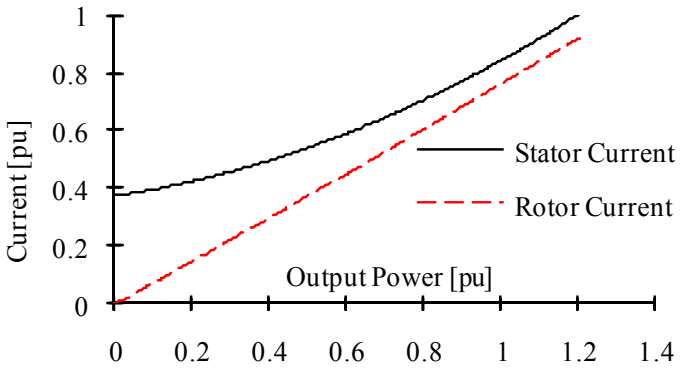

(a)

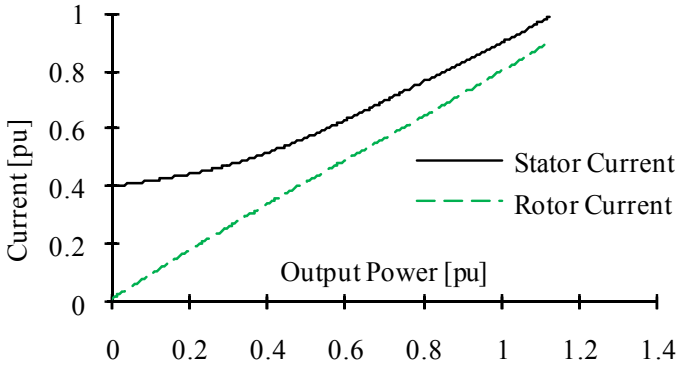

(b)

Fig. 3.21. Measured maximum output power at rated stator current, stator voltage and speed for both CRSEIG and ALSEIG. (a) CRSEIG. (b) ALSEIG.

Figures 3.22(a) and (b) show the variation in VAR requirement and the capacitive reactance for both the machines to keep a rated terminal voltage across the stator terminals at the rated speed of the machines under varying loads. It was observed that the no-load excitation requirement of the CRSEIG was a bit more than the ALSEIG. As the

machines were loaded the VAR and the capacitance required by the ALSEIG was more than that of the CRSEIG. The range of capacitance requirement for CRSEIG varied from 37μF to 55 μF, whereas the same for ALSEIG varied from 65 μF to 87 μF, for no-load to maximum loading condition. It is also seen that the compensating capacitance requirement of the CRSEIG is reduced due to the design of the machine with higher value of flux density. Otherwise, the lesser capacitance requirement for the CRSEIG can be attributed to the steeper saturation characteristics of the machine.

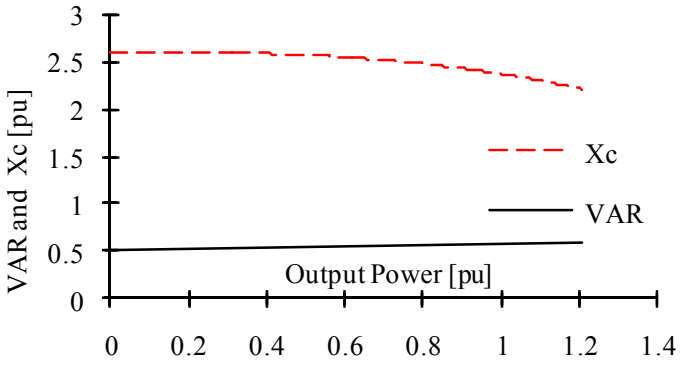

(a)

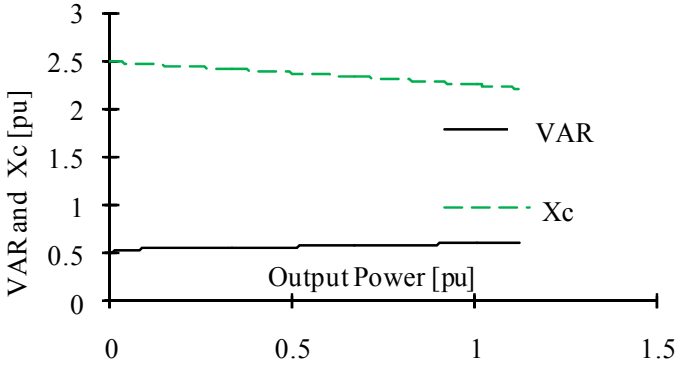

(b)

Fig. 3.22. Measured reactive power (VAR) requirement and capacitive reactance (Xc) at rated stator voltage and speed for both CRSEIG and ALSEIG during incremental loading of the machines. (a) CRSEIG. (b) ALSEIG.

Figure 3.23 shows the measured saturation characteristics of both the machines at rated frequency. An economical SEIG system would be the one which uses a lesser range of capacitance to reach the maximum power. Considering the above statement, the CRSEIG

needs a lower range of capacitance for higher power output than the ALSEIG.

Figure 3.24 shows the variation in terminal voltage with output power for capacitance values of 37μF and 65 μF for CRSEIG and ALSEIG respectively, measured across the stator terminals, while run at their respective rated speed. These capacitance values are corresponding to rated voltage at rated speed and no-load for the machines. It is apparent from these figures that the voltage drop increases as the loading increases. This is due to the fact that with more loading, the operating slip has to be more negative and therefore, at the same rotor speed, the stator frequency becomes lesser. Consequently, the magnetizing characteristic shifts downwards but the capacitive reactance increases.

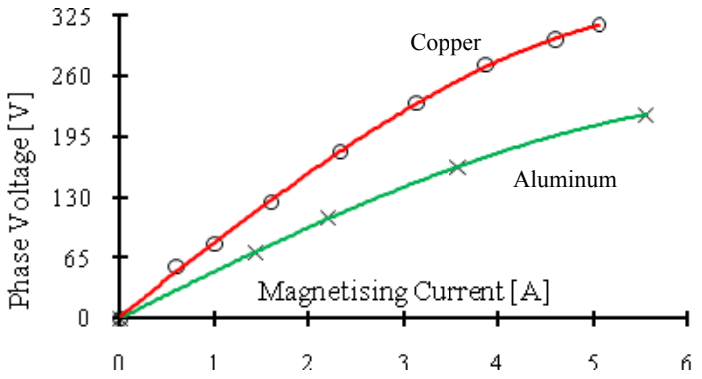

Fig. 3.23. Measured saturation characteristics of aluminum- and copper-rotor machines at their rated frequency.

Finally, therefore, the operating point of intersection of the capacitor *V-I* characteristic and the new magnetization characteristic corresponds to a lesser terminal voltage at a higher loading at steady state.

The voltage regulation for the aluminum-rotor machine has been found to be better than that of the copper-rotor machine. As a load is applied, the VAR supplied by the capacitance of the parallel combination of the excitation capacitance and the connected load must match the VAR demanded by the machine as dictated by the magnetizing curve. In other words, the VAR, required by the machine to maintain self-excitation and the load must be provided solely by the excitation capacitor. Consequently, as the load is increased, there is a decrease in the magnitude of the terminal voltage and frequency.

As the load becomes more inductive, the VAR that can be supplied by the capacitors

is distributed between the machine and the load. Consequently, the VAR available to the machine is less than the open-circuit conditions. Hence, the voltage decreases further. This is the reason why the induction machine has the ability to protect itself from overloading current. The value of the magnetizing reactance plays an important role for safe operation of the SEIG. Since, the magnetizing curve of the copper-rotor SEIG is steeper than the aluminum-rotor machine studied in these investigations, for each unit decrease in the magnetizing current, the decrease in voltage is more in the case of copper-rotor SEIG in comparison to the aluminum-rotor SEIG.

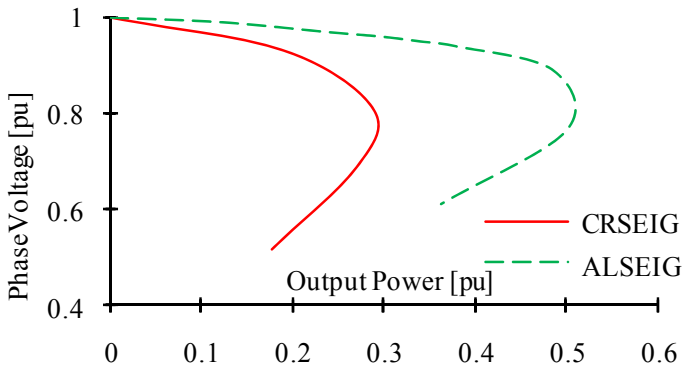

Fig. 3.24. Measured voltage regulation characteristics for CRSEIG and ALSEIG at rated speed and capacitance of 37μF and 65 μF.

Figures 3.25 (a) and (b) show the variation of terminal voltage with respect to the output power for different values of mechanically-switched capacitor used in these investigations. From the figures, it can be observed that the for about 6% variation in terminal voltage from the rated value, the CRSEIG, because of its poor voltage regulation, required almost seven steps of capacitor switching to generate the maximum power. Whereas, the ALSEIG required only about four capacitor switching steps to reach its maximum power. Hence, the voltage regulating scheme will be a lot cheaper for the ALSEIG compared to that of the CRSEIG. From the above, it can be concluded that since the SEIG is desired to operate near its rated power almost all the time, the ALSEIG used in this investigation may not require any voltage regulation if a 6% variation in terminal voltage is permitted.

Also, the ALSEIG will require lesser range of capacitance to reach it maximum

loading condition keeping in view the stipulated voltage regulation limit.

The terminal frequency of both the machines under incremental loading condition was also measured. Primarily, it should be noted that the change in frequency is found to be roughly proportional to the change in terminal voltage of the machine at *R* load, i.e., there is a similarity in the trend of change in terminal voltage and frequency. It is also observed that the change in frequency for the copper-rotor machine is less than that of the aluminum-rotor machine. Stator frequency of the CRSEIG and ALSEIG dropped to 0.989 pu and 0.982 pu under full load condition, respectively. It is also seen that the copper-rotor machine takes less time to regain a stable frequency during resistive loads and more time than the aluminum-rotor machine at inductive loads.

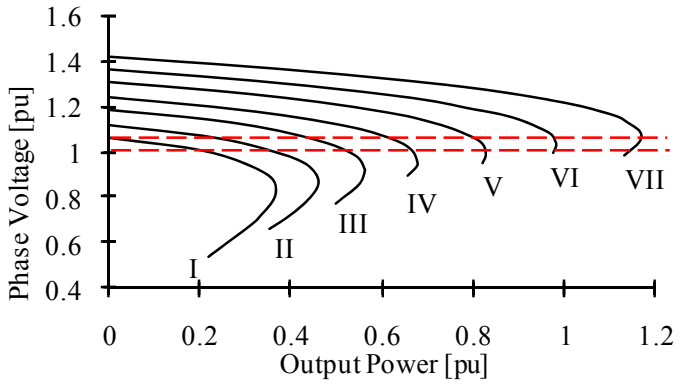

(a)

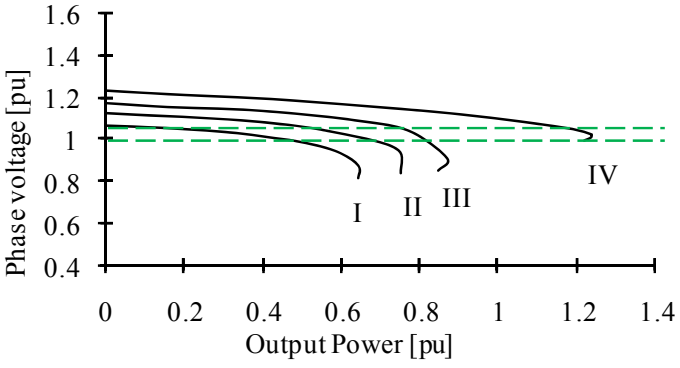

(b)

Fig. 3.25. Measured voltage regulation characteristics at rated speed for both CRSEIG and ALSEIG.

(a) **CRSEIG:** Capacitance: (I) 38 µF (II) 40 µF (III) 42 µF (IV) 44 µF (V) 47 µF (VI) 49 µF (VII) 54 µF

(b) **ALSEIG:** Capacitance: (I) 69 µF (II) 72 µF (III) 76 µF (IV) 84 µF

4.0 A NOVEL LOW-COST MODULE BASED ON DAUBECHIES WAVELET TRANSFORMS AND SWARM INTELLIGENCE TECHNIQUE FOR VOLTAGE REGULATION IN SEIGs

4.1 Introduction

The study performed above, calls the need for voltage regulation (VR) in the SEIG. VR schemes can be largely classified into shunt compensation and series compensation schemes. Each of the above schemes can be further classified into classical, switching device based and converter based schemes. [1] and [2] propose VR schemes employing switched controlled inductor and switched shunt capacitors respectively. Research performed in [3], [4] use the static VAR compensator for VR. Converter based shunt compensation VR schemes like static synchronous compensator (STATCOMs) based on voltage source converters (VSCs) and current source converter based shunt compensation are presented in [5], [6]. Various converters based, switching devices based and constant voltage transformer based series compensation schemes are studied in [7]-[11].

Therefore, an effective capacitive VAR controller has become central to the success of SEIG system for stand-alone applications. Reactive power may be provided by switched capacitors, static VAR compensator (SVC), and STATCOM. A switched-capacitor scheme is cheaper, but it regulates the terminal voltage in discrete steps. Electromechanical switches are found to cause unstable chattering and solid state switching needs correct timing. Static VAR compensator uses either thyristor-switched capacitor (TSCs) or a thyristor-controlled reactor (TCR) with fixed capacitor. As stated in [11] an electronic load controller is used as a VR scheme in microhydro application, however, this method is not economically viable for other applications involving inductive loads and needing voltage regulation [8]-[11]. The static VAR compensators reported in [12] is understood to be a popular VR scheme but it pulls down its merits due to its expensive sized capacitors, inductors and injection of harmonics into the system. STATCOM [13]–[16] employs a voltage source inverter, which internally generates capacitive/inductive reactive power. STATCOM-based systems have initially proposed for reactive power compensation and power factor correction in utility systems [17]–[23].

Larsen *et al.* [17] have described the benefits of STATCOM over the SVC system. They have shown that the steady state, as well as transient performance, can be improved with STATCOM.

Understanding the complexity, economics of the above schemes and the need for VR in SEIG, a highly efficient, responsive and cost-effective wavelet/PSO based VR scheme is proposed and interfaced with a switched capacitor based voltage regulator. Since, the proposed module is based on detection of changing load and stator current transients, the VR scheme remains effective, regardless of changes in system parameters. Current-acquisition devices are generally integrated in an DWPG for monitoring and control purposes, therefore, no additional sensors are needed for the operation of this module and hence, hardware cost is decreased [24].

The VR scheme was developed keeping in mind the future scope of integrating this wavelet/PSO based module with a STATCOM for higher resolution and better voltage regulation. However, in order to illustrate the developed VR scheme at a laboratory level switched capacitor banks have been used.

A Wavelet, which has energy concentrated in time, is well-suited to analyse the transient and non-stationary or time-varying phenomena. Wavelet transform can be divided into continuous wavelet transforms (CWT) and discrete wavelet transforms (DWT). A DWT based methodology is chosen here as it has excellent signal compaction properties for a variety of real-world signals while being computationally very efficient. The transient is recognized within 1 ms, which allows the system to estimate and respond to the changing load current, stator current and voltage, instantly. In a DG, the central controller regulates various power generating devices simultaneously, therefore, it involves multiple task management and complex calculations. The developed wavelet based transient detection unit is capable of detecting load application independently, which significantly decreases the complexity of the controller.

Since, the proposed module is based on detection of changing load and stator current transients, the VR scheme remains effective, regardless of changes in system parameters. Additionally, any voltage regulator previously discussed in this section can be implemented using the same Wavelet/ PSO control scheme, thus making it more reliable and flexible.

4.2 Voltage Regulation Scheme Using Wavelet/PSO Based Embedded System Interfaced With Switched Capacitor Bank

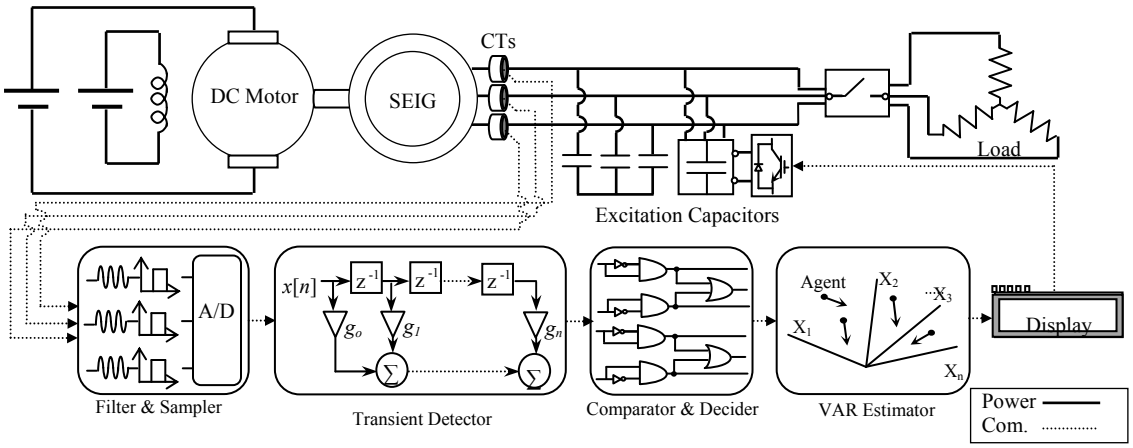

Fig. 4.21. Overall block diagram of the developed wavelet/PSO based embedded system integration with the SEIG and the Switched capacitor bank system used in this research.

Fig. 4.21 shows the overall block diagram of the developed wavelet/PSO based embedded system integration with the SEIG and the switched capacitor bank system used in this research. Detailed explanation of each block is given below.

C. Wavelet based Transient Detector

A1) Introduction to discrete wavelet analysis and Daubechies wavelet

A wavelet is a mathematical function used to divide a given function or continuous-time signal into different scale components, assigning a frequency range to each scale component. Wavelets not only dissect signals into their component frequencies but also vary the scale at which the component frequencies are analyzed. Thus, wavelets, as component pieces used to analyze a signal, are limited in space [25]-[29]. A wavelet transform (WT) is the representation of a function by wavelets. The wavelets are scaled and translated as copies (known as "daughter wavelets") of a finite-length or fast-decaying oscillating waveform (known as the "mother wavelet") [25]-[28]. Unlike the Fourier transform, wavelet transform does not need a single set of basis function [26], [27]. Instead, wavelet transforms have an infinite set of possible basis functions. Thus, wavelet analysis provides immediate access to information that can be obscured by other

time frequency methods such as the Fourier analysis. It can be broadly classified into continuous and discrete wavelets.

A2) Continuous wavelet transforms

The continuous wavelets, represented on a frequency band of the form [*f*, 2*f*] for all positive frequencies [*f*>0] are scaled by factor 1. The subspace is generally obtained by shifting the mother wavelet. The subspace of scale '*a*' or frequency band [1/*a*, 2/*a*] is generated by the functions :

$$\psi_{a,b}(t) = \frac{1}{\sqrt{a}}\psi\left(\frac{t-b}{a}\right) \tag{4.21}$$

where, '*a*' is the scale factor, '*b*' denotes the shift factor and $\Psi_{a,b}(t)$ is defined as the mother wavelet [26], [27].

A3) Discrete wavelet transforms

The continuous wavelets are converted into discrete domain for real-time implementation. One such system is the affine system for real parameters *a*>1, *b*>0.

$$\psi_{m,n}(t) = a^{-\frac{m}{2}}\psi(a^{-m}t - nb) \tag{4.22}$$

$$x(t) = \sum\sum \alpha \left\langle x, \psi_{m,n} \right\rangle, \psi_{m,n}(t) \tag{4.23}$$

The discrete subset of the half-plane consists all the points (a^m, $na^m b$) with integers *m*, *n* belongs to a set of integers. The corresponding mother wavelet is given in (4.22).

$$DWT(m,n) = 2^{-\frac{m}{2}} \sum\sum x(n)\psi\left(\frac{t - n2^m}{2^m}\right) \tag{4.24}$$

A sufficient condition for the reconstruction of any signal *x* of finite energy is given by (4.23). $\Psi_{m,n}$ is the discrete mother wavelet respectively. The discrete wavelet transform (DWT) is defined in (4.24).

The discrete wavelet is an orthonormal transform; the *n*th wavelet coefficient W_n is associated with a particular scale and with a particular set of times. The DWT of a signal

$x[n]$ is defined as its inner product with a family of functions, $\varphi_{j,k}(t)$ and $\psi_{j,k}(t)$ [25] as shown below:

$$\left.\begin{aligned}\varphi_{j,k}(t) &= 2^{j/2}\varphi(2^j t-k)\\ \psi_{j,k}(t) &= 2^{j/2}\psi(2^j t-k)\end{aligned}\right\} \tag{4.25}$$

The functions $\varphi(t)$ and $\psi(t)$ are scaling and wavelet functions, which are descretized at level j and at translation k. For the implementation of the DWT, only the coefficients of two half-band filter: a low-pass $h(k)$ and a high-pass $g(k) = (-1)^k h(1-k)$ filter, are required, which satisfy the following conditions [25]:

$$\left.\begin{aligned}\varphi_{j+1,0}(t) &= \sum_k h[k]\cdot\varphi_{j,k}\\ \psi_{j+1,0}(t) &= \sum_k g[k]\cdot\psi_{j,k}\end{aligned}\right\} \tag{4.26}$$

Hence, the corresponding DWT is:

$$\left.\begin{aligned}A_{j+1,n} &= \sum_k A_{j,k}\cdot h_j[k-2n]\\ D_{j+1,n} &= \sum_k A_{j,k}\cdot g_j[k-2n]\end{aligned}\right\} \tag{4.27}$$

A wavelet filter $\{h_l : 0, 1, \ldots, L\text{-}1\}$ for an infinite sequence with at most L nonzero values must satisfy the following three basic properties [30]:

$$\left.\begin{aligned}&\sum_{l=0}^{L-1} h_l = 0;\\ &\sum_{l=0}^{L-1} h_l^2 = 1;\\ &\sum_{l=0}^{L-1} h_l h_{l+2n} = \sum_{l=-\infty}^{\infty} h_l h_{l+2n} = 0;\end{aligned}\right\} \tag{4.28}$$

for all the nonzero value n.

By imposing an appealing set of regularity conditions, Daubechies (Db) came up with a useful class of wavelet filters, all of which yield a DWT in accordance with the notion of difference of adjacent averages. Daubechies wavelet is deemed most used mother wavelet

in power system studies due to its orthogonal property, which is potent for localization and classification of disturbances. In comparison to other orthogonal wavelet like Haar and Symlet, Db gives higher yield in terms of computation complexity and filter response [31].

Choosing the best Daubechies wavelet is of paramount importance to overcome constraints like computation time, localization efficiency and classification. The differences in filters are mainly due to the length of the filters that defines the wavelet and scaling functions.

Comparison of Db2 to Db10 wavelet showed that a wavelet becomes smoother with increase in coefficient numbers. Db2 and Db6 presented a more severe transition at the start of the event than at the end. This fact was only observed in Db2 and Db6 wavelets, that selected the beginning and the end of the disturbance according to the value of the wavelet coefficients. The wavelet coefficients relating to the beginning of the event (less rapid transition) presented absolute value greater than the wavelet coefficients of the end of the event. Therefore, Db2 and Db6 wavelet were more selective [31]. Where in comparison, Db6 showed proportionate response at the beginning and end of the event. Thus, for the purpose of all-round performance Db6 was selected for this study. Fig. 4.22 demonstrates the implementation of Daubechies 6 decomposition 11th order FIR high pass filter, coefficients of which is shown in Table II.

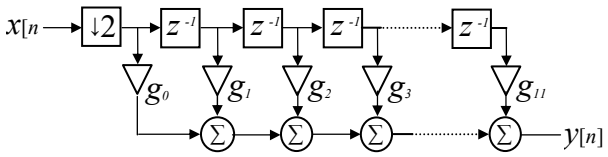

Fig. 4.22. Finite impulse response filter for wavelet decomposition.

TABLE II
HIGH-PASS FINITE IMPULSE RESPONSE COEFFICIENTS

Order	Coefficients	Order	Coefficients
g_0	-0.1115407434	g_6	-0.0975016056
g_1	0.4946238904	g_7	0.0275228655
g_2	-0.7511339080	g_8	0.0315820393
g_3	0.3152503517	g_9	0.0005538422
g_4	0.2262646940	g_{10}	-0.0047772575
g_5	-0.1297668676	g_{11}	-0.0010773011

A2) Transient detection using wavelet transforms

Current sensors connected to the 3-phase power line are used to acquire instantaneous current amplitude which is later fed to the wavelet transient detection unit as a voltage signal. Fig. 4.23 illustrates the waveforms captured through a Tektronix digital oscilloscope during load application. Extensive studies on the current-pattern of the system show that transients at the range of 4-10 kHz are dominant during load perturbation and stator current variation. This range of frequency contains a lot of information required to capture the transients. A second order multiple feedback (MFB) band pass filter as shown in Fig. 4.24, is designed to remove unnecessary information from the signal and retain the high frequency information.

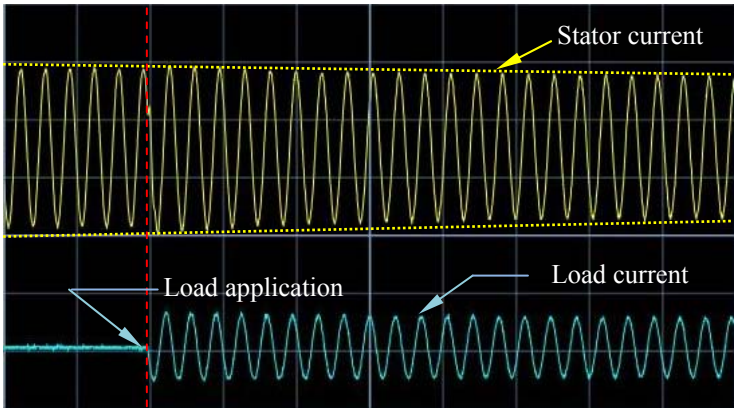

Fig. 4.23. Stator current and load current profiles obtained through 1000:1 turns ratio current sensor without capacitor compensation.

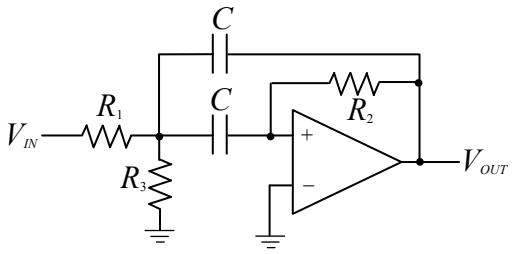

Fig. 4.24. Second-order multiple feedback bandpass filter.

The transfer function of the MFB band-pass circuit is shown in (4.29).

$$A(s) = \frac{-\frac{R_2 R_3}{R_1 + R_3} C\omega_m s}{\frac{R_1 R_2 R_3}{R_1 + R_3} C^2 \omega_m{}^2 s^2 + \frac{2R_2 R_3}{R_1 + R_3} C\omega_m s + 1} \tag{4.29}$$

where, ω_m is the mid-angular frequency of the filter.

The filtered signal is now sampled according to the Shannon's theorem, which states that, an Ω-band limited function can be reconstructed completely from its values:

$$(f(kT) \mid k \in Z), T := \frac{\pi}{\Omega} \tag{4.30}$$

sampled at the discrete points *kT*. All the harmonic components occurring in *f* have a period length ≥ 2π/Ω. Thus, by requiring $T := \pi/\Omega$, one makes sure that any pure oscillation possible present in *f* would be sampled at least twice per period. The sampling frequency, therefore, is chosen as 20 kHz for this work [32].

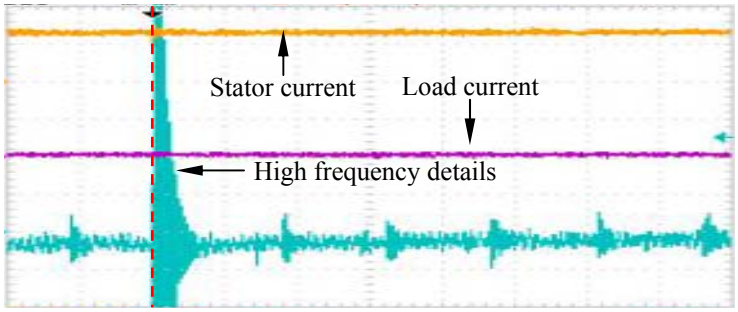

Fig. 4.25. Measured high frequency waveforms obtained as output voltages of the band pass filter stage during load application.

Fig. 4.25 shows the sampled data obtained out of the MFB filter as high frequency waveforms during load application. As seen from Fig. 4.25, the blue spike shows the measured high frequency transient waveform during load application. It can also be observed that the changes in the load and stator current are indecipherable due to the high sampling rate used in the measurement.

The filtered signal is then sampled with a sampling frequency f_s at 20 kHz based on Nyquist`s criterion to ensure proper reconstruction of the signal. The filtered and sampled

data is passed through a discrete wavelet decomposition block. The input signal is re-filtered to differentiate various other high frequency details in the system and capture the information just required for VR through conditional threshold selection performed by the comparator and decider block. This difference in the input and output of this block is illustrated in Fig. 4.26 and Fig. 4.27 through measured and calculated results.

According to [31], the window of usable data is limited to 3 ms due to the Current Transformer saturation during sub-transient and transient currents. The high frequency details of all three phases collected during VR, namely HF_a, HF_b, and HF_c, obtained after wavelet decomposition are continuously checked for signals above threshold values (VR_{Th}) for each phase. Extensive theoretical and experimental investigations were performed to obtain the thresholds for voltage regulation under different loading conditions, excitation capacitances and speeds of the rotor, for both aluminum- and copper-rotor SEIGs. Hereafter, this block would activate the successive PSO based VAR estimator through a control signal to compute the amount of capacitance required for proper voltage regulation.

A3) Implementation of the wavelet based transient detector on a low cost embedded system

The transient detection block using wavelet transform is implemented and tested in this section using a low-end embedded system. This system consists of three 16-bit digital signal controllers DsPIC33F DCS, with 40 MIPS capability and up to 80 MHz speed with a Phase-Locked Loop (PLL). These chips have their own digital signal processor engine capable of conducting single cycle multiplication and accumulation. In order to ensure a stable system, the transient detection unit traces stability for 250 consecutive samples. The prototype was tested for voltage regulation where in a static load was applied across the stator terminals of the aluminum-rotor SEIG at periodic intervals in order to test the reliability of module under different conditions, initial excitation capacitances and different phase angles of stator current. Fig. 4.26 shows that the trigger was applied at different phase angles i.e. negative and positive half cycles and the module was efficient enough to identify the transient and capture high frequency transient information at all instances.

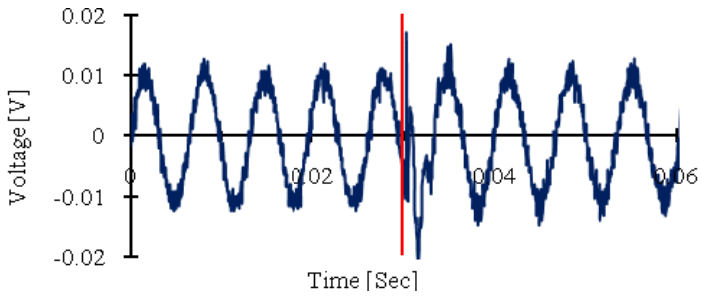

(a)

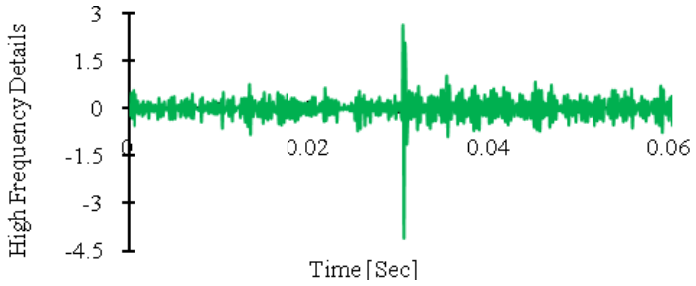

(b)

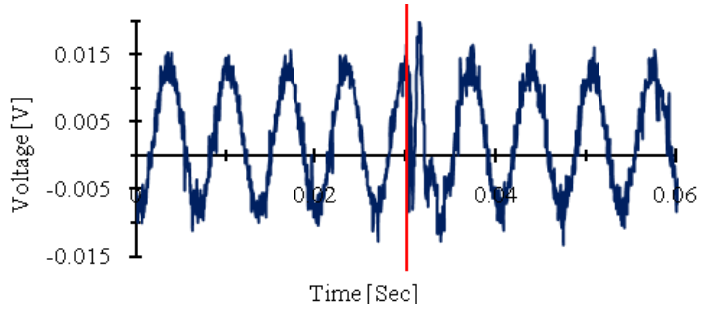

(c)

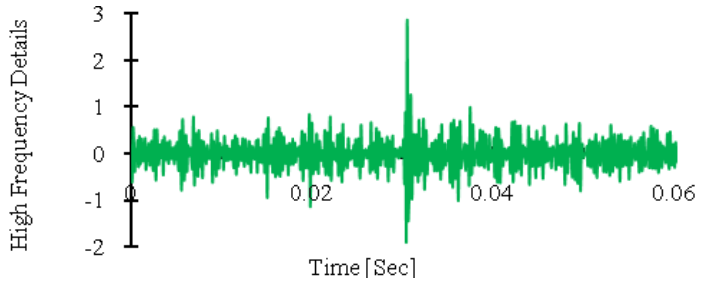

(d)

Fig. 4.26. Experimental results for voltage regulation. (a) Second-order MFB bandpass filter output for load applied at negative half cycle of stator current signal. (b) Wavelet decomposition output corresponding to (a). (c) Second-order MFB bandpass filter output for load applied at positive half cycle of stator current signal. (d) Wavelet decomposition output corresponding to (c).

Figs. 4.26(a) and 4.26(c) show the experimental output data of the bandpass filter which is sampled and stored in the DsPIC33F DCS. Corresponding high frequency details obtained from experiments are shown in Fig. 4.26(b) and Fig. 4.26(d). The entire voltage regulation test process explained above was also simulated using a developed computer program for the aluminum-rotor SEIG and the corresponding calculated results are shown in Fig. 4.27. The transient or the high frequency spike at 0.03 seconds is remarkably distinguishable which enables to choose a specific threshold for voltage regulation.

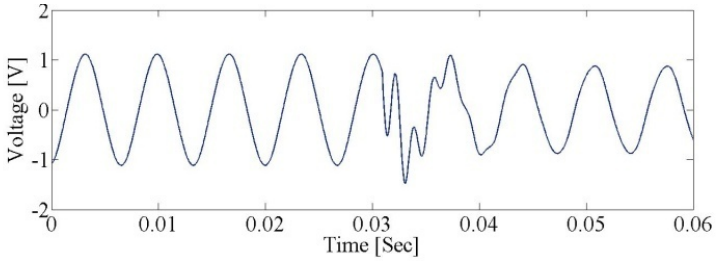

(a)

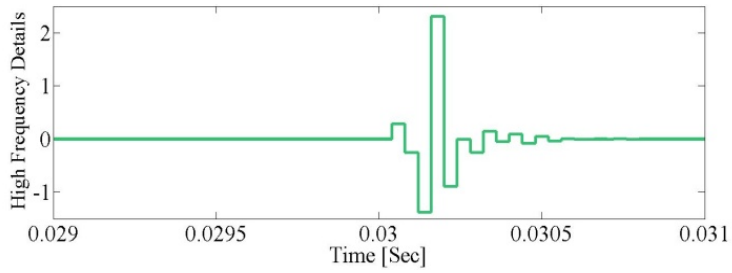

(b)

Fig. 4.27. Calculated results for voltage regulation. (a) Second order MFB bandpass filter output for load applied at positive half cycle of stator current signal. (b) Corresponding wavelet decomposition output.

The VR can be achieved using any type of power electronic hardware as stated above. However, in order to validate this wavelet/PSO based VR scheme, a switched capacitor scheme for voltage regulation has been illustrated in this research thesis. The proposed VR scheme is applicable to almost any system as it is based on the universal principle of change of capacitance to achieve voltage regulation. The authors' would like to reiterate that the system is proposed only as a validation scheme for the module's transient detection and VAR estimation capabilities. Hence, a simple power switch has been used to enable switching of the capacitors. This scheme can be extended to Static VAR

compensators, Hybrid VAR compensators, TSCs and TCRs and other FACTS controllers that enable continuous change of capacitance instead of switching them in steps. But this can be done at the cost of control mechanisms for monitoring firing angle delay.

The scheme proposed involves a low power gate drive signal from the 8-bit master controller which triggers the power switch. The master unit of the wavelet is capable of sending digital/analog output used for selecting different values of capacitances to achieve different levels of voltage regulation at different loads. The compensation capacitance value determines the bit pattern of the master's output. The 5 V gate trigger is enough to drive a power switch. In case of hard driven power switches, an amplifier may be employed to the system after a *V-I* converter or an Op-Amp based on the requirement of a drive voltage or current. The principle behind estimating the capacitance is explained in the following section.

D. VAR Requirement Estimator Using Particle Swarm Optimization

The two-axis model of SEIG, as shown in chapter 2, is developed using machine equations based on the dq reference frame theory in order to bring out the performance of the SEIGs under various loading conditions such as *R* and *RL* loads. The previously developed mathematical model of SEIG is used here for VAR estimation.

B1) Mathematical modeling of Particle Swarm Behavior

The PSO based VAR estimator is activated once a load changing transient is detected by the wavelet transient detector. This unit uses the developed mathematical models of the SEIG and the PSO to estimate the VAR precisely. Hence, the capacitance value required to provide the necessary VAR at the machine terminals will be calculated.

The PSO simulates the behavior of swarm as a simplified social system. Each particle modifies its velocity according to its own position and the positions of neighbors in the following form:

$$\begin{aligned} v_i^{k+1} &= v_i^k + c_1 \times rand_1 \times (pbest_i - s_i^k) \\ v_i^{k+1} &= v_i^k + c_2 \times rand_2 \times (gbest_i - s_i^k) \end{aligned} \tag{4.31}$$

where, v_i^k is the velocity of particle i at iteration k, c_j is weighting coefficient, $rand_i$ is a random number between 0 and 1, s_i^k is the current position (capacitance value) of particle i at iteration k, $pbest_i$ is the best previous position of the i_{th} particle, $gbest_i$ represents the best previous position among all the particles in the swarm [33, 34].

Aggregating the set of equations in (4.31), the velocity of the i_{th} particle can be modified as follows:

$$\begin{aligned} v_i^{k+1} = wv_i^k + c_1 \times rand_1 \times (pbest_i - s_i^k) \\ + c_2 \times rand_2 \times (gbest_i - s_i^k) \end{aligned} \tag{4.32}$$

where, w represents weighting function which is usually utilized in (4.33):

$$w = w_{\max} - \left[\frac{w_{\max} - w_{\min}}{iter_{\max}} \times iter \right] \tag{4.33}$$

where, w_{max} is the initial weight, w_{min} is the final weight, $iter_{max}$ is the maximum iteration number, and $iter$ is the current iteration number.

PSO utilizes *pbest* and *gbest* to modify current searching point. With equations (4.32) and (4.33), a certain velocity that converges gradually towards *pbest* and *gbest* can be calculated, which is called Inertial Weights Approach (IWA). The current position can be, therefore, modified by the following equation:

$$s_i^{k+1} = s_i^k + v_i^{k+1} \tag{4.34}$$

According to Shi and Eberhart's examination [35, 36], $c_i = 2.0$, $w_{max} = 0.9$, $w_{min} = 0.4$ are appropriate parameters as these values do not depend on any particular problem.

In order to keep a constant terminal voltage of the machine, the objective function is chosen as:

$$e = | V_t - V_{t\_rated} | \tag{4.35}$$

where, V_t is the calculated terminal phase voltage of the developed two-axis model of SEIG, V_{t_rated} is the rated phase voltage of the SEIG which equals to 265 V for the copper-rotor machine under consideration. The objective for particle swarm is to minimize the e which indicates the error. The steps involved in estimating the best

capacitance value are described as follows:

Step 1. Generation of initial conditions: Initialize population size N, maximum iteration number $iter_{max}$, and other PSO parameters. Randomly generate the initial trial particles s_i (i =1, 2, …, N, where N is the population size) which indicate the possible solutions of capacitance value.

Step 2. Computation of objective function: Capacitance values are fed into the developed two-axis model of the SEIG to calculate the output voltage of the generator. The error of each agent can be attained with (4.35).

Step 3. Evaluation of searching point: If e is smaller than the current *pbest* of the agent, the *pbest* value is replaced by the current value. If the smallest e of *pbest* is smaller than the current *gbest*, *gbest* is replaced by the best value.

Step 4. Modification of the searching point: The current capacitance value of each agent is changed using (4.32)-(4.34).

Step 5. Checking the exit condition: When the current iteration number reaches the predetermined maximum iteration number or if the error is lesser than 0.1, then exits. Otherwise, the process goes back to Step 2.

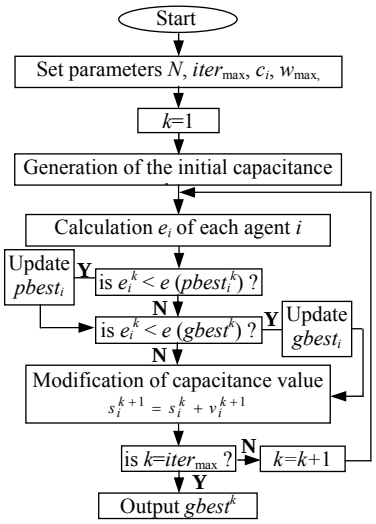

Fig. 4.28. Flowchart of the step by step process involved in calculating the capacitance using the SEIG-PSO algorithm.

B2) Testing of the PSO algorithm

Figure 4.28 shows the flowchart of the proposed PSO based capacitance estimation

method. The proposed estimator is tested under *RL* loading condition. The population size *N* of the swarm and iteration time $iter_{max}$ are 20 and 40, respectively. Fig. 4.29 shows the searching points of particle 1 which keeps on "flying" and "exploring" to converge to the most suitable value.

Varied loads were applied to further verify the convergence of the developed optimization method. From Fig. 4.30, it is evident that the PSO performance is satisfactory after 30 iterations for all the tested loading conditions.

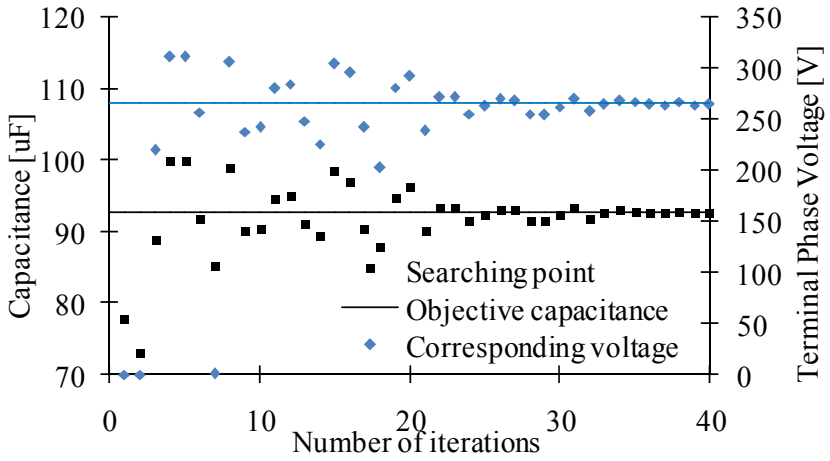

Fig. 4.29. Searching points and terminal phase voltage of particle 1 obtained from numerical investigations under a load of R=30 Ω and X_L=22.5 Ω.

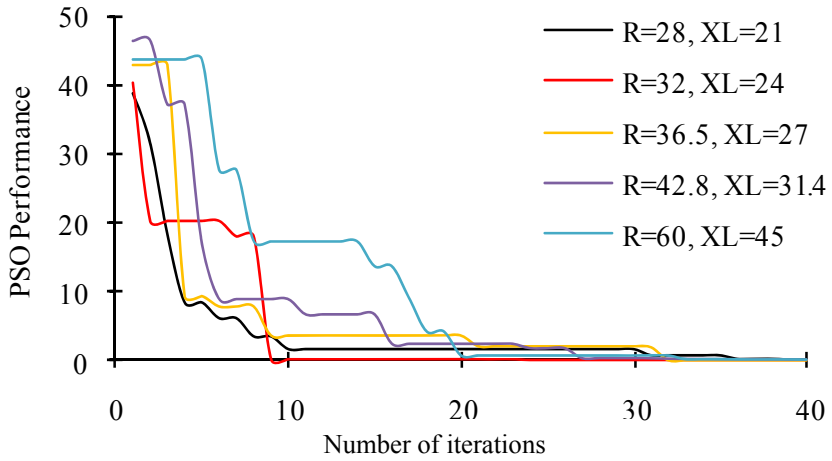

Fig. 4.30. PSO performance (estimated error) as a function of iteration time for varying loading conditions.

The value of compensation capacitor can be further explained with current I_{com} as:

$$I_{com} = \frac{V_t}{(X_{c\_total} - X_c)} \tag{4.36}$$

where, X_{c_total} is the estimated reactance requirement of SEIG after load application. X_c is the reactance of shunt capacitor connected in the system to build up the no-load voltage.

Going a step further to show the voltage regulation achieved through this overall module, copper-rotor SEIG was loaded at around 29 seconds after it reached its steady state. The module detected the transient during load application and enabled the power switch through the control signal to switch the compensating capacitances and sustain the original voltage.

The amount of capacitance needed to be switched was also shown on the LCD used in the experimental setup. Fig. 4.31 shows the measured results obtained from a Fluke Power Quality Analyzer and the corresponding calculated results are shown in Fig. 4.32.

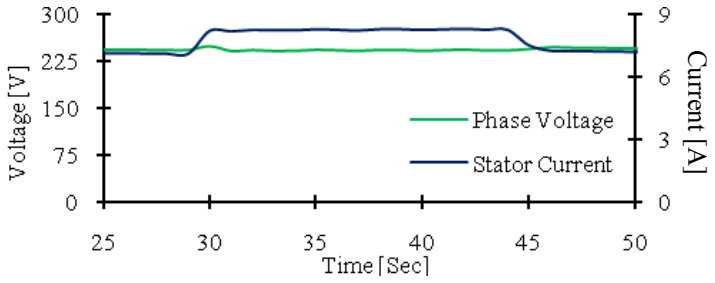

(a)

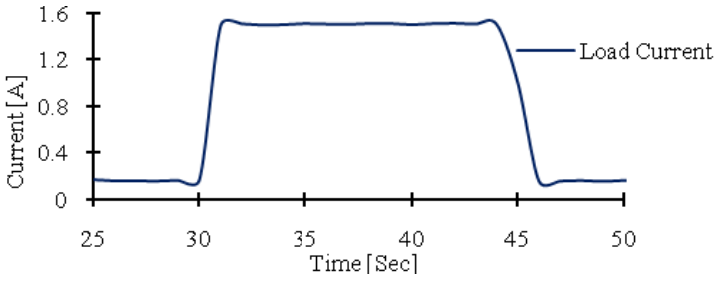

(b)

Fig. 4.31. Measured results for voltage regulation using switched capacitor scheme. (a) Stator voltage and current profiles on load application and removal. (b) Corresponding load current profile.

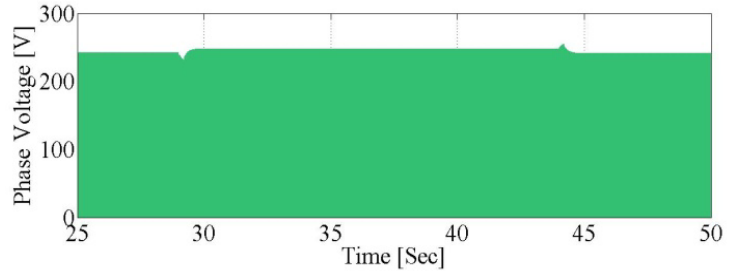

(a)

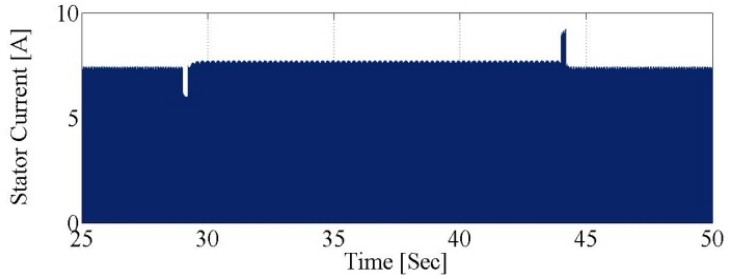

(b)

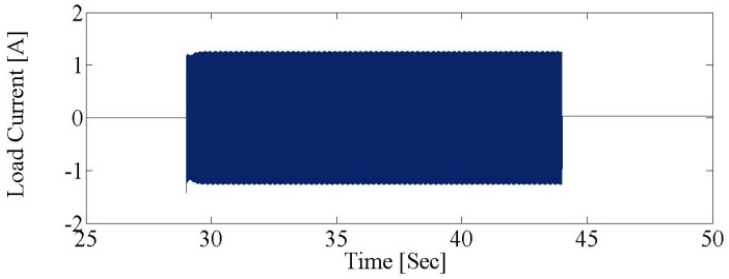

(c)

Fig. 4.32. Calculated results for voltage regulation using switched capacitor scheme. (a) Stator voltage and current profiles on load application and removal. (b) Corresponding load current profile.

We can see from the experimental results that a small transient is seen around 30 seconds during the application of load and then the voltage stabilizes back to its original value. Load was switched off at around 44 seconds and we see that the voltage increases for a few milliseconds and decreases back to its pre-transient level due to the switching of new capacitance value. Fig. 4.33 shows the experimental setup of the wavelet/PSO based module.

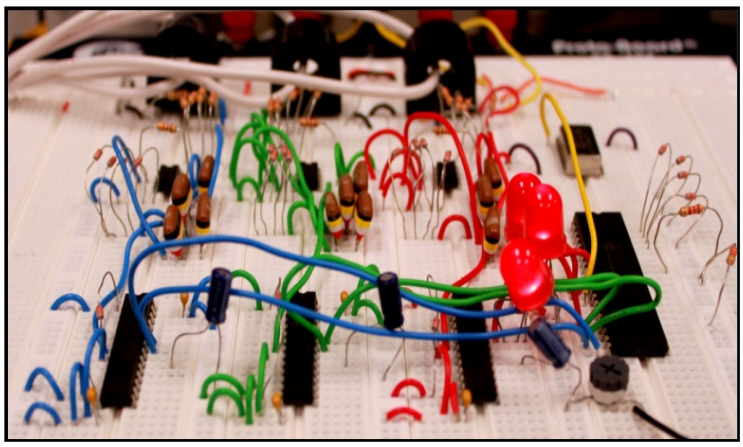

Fig. 4.33. Experimental setup of the wavelet/PSO based module.

4.3 References

[1] E. C. Quispe, R. D. Arias, and J. E. Quintero, "A new voltage regulator for self-excited induction generator-design, simulation, and experimental results," in Proc. IEEE Conf. Elec. Mach. Drives, pp. TB3/7.1-TB3/7.3.

[2] H. C. Rai, A. K. Tandan, S. S. Murthy, B. Singh, and B. P. Singh, "Voltage regulation of self-excited induction generator using passive elements," in Proc. IEEE Int. Conf. Elec. Mach. Drives, 1993.

[3] D. K. Jain, A. P. Mittal, and B. Singh, "Advanced controlled series compensated self-excited induction generator," in Proc. Int. Conf. Power Elect. Drives Energy Syst. Ind. Growth, 1996, pp. 707–712.

[4] T. Ahmed, O. Noro, E. Hiraki, and M. Nakaoka, "Terminal voltage regulation characteristics by static Var compensator for a 3-phase self-excited induction generator," IEEE Trans. Ind. Appl., vol. 40, no. 4, pp. 978–988, Jul./Aug. 2004.

[5] B. Singh and L. B. Shilpakar, "Analysis of a novel solid state voltage regulator for a self-excited induction generator," Pro. of Ins. Elect. Eng. Gen. Tra. Dist., vol. 45, no. 6, pp. 647–655, Nov. 1998.

[6] B. Singh and G. K. Kasal, "Neural network-based voltage regulator for an isolated asynchronous generator supplying three-phase four-wire loads," Elect. Power Syst. Res., vol. 78, no. 6, pp. 985–994, Jun. 2008.

[7] K. K. Sen, "SSSC—Static synchronous series compensator: Theory, modelling, and applications," IEEE Trans. Power Del., vol. 13, no. 1, pp. 241–246, Jan. 1998.

[8] R. Bonert and G. Hoops, "Stand alone induction generator with terminal impedance controller and no turbine controls," IEEE Trans. Energy Convers., vol. 5, no. 1, pp. 28–31, Mar. 1990.

[9] R. Bonert and S. Rajakaruna, "Self excited induction generator with excellent voltage and frequency control," Proc. of Inst. Elect. Eng. Gen., Tran. and Dist., vol. 145, no.1, pp. 33-39, Jan. 1998.

[10] D. Henderson, "An advanced electronic load governor for control of microhydro electric generation," IEEE Trans. Energy Convers., vol. 13, no. 3, pp. 300–304, Sep. 1998.

[11] B. Singh, S. S. Murthy, and S. Gupta, "Analysis and implementation of an electronic load controller for self-excited induction generator," Proc. of Inst. Elect. Eng.—Gen. Tran.and Distr., vol. 151, pp. 51–60, 2004.

[12] M. B. Brennen and A. Abbondanti, "Static exciters for induction generators," IEEE Transactions Industrial Application, vol. IA-13, pp. 422–428, Dec. 1977.

[13] B. Singh, S. S. Murthy, and S. Gupta, "Analysis and Design of STATCOM based voltage regulator for self excited induction generator," IEEE Trans. on Energy Conversion, vol. 19, no.4, pp. 783-790, Dec. 2004.

[14] E. G. Marra and J. A. Pomilio, "Self-excited induction generator controlled by a VS-PWM converter providing high power-factor current to a single-phase grid," in Proc. Industrial Electronics Society Conf., 1998, pp. 703–708.

[15] S. C. Kuo and L. Wang, "Analysis of voltage control for a self excited induction generator using a current-controlled voltage source inverter (CC-VSI)," Proc. Inst. Elect. Eng., Gen., Transm. Distrib., vol. 148, no.5, pp. 431–438, Sept. 2001.

[16] H. Akagi, Y. Kanazawa, and A. Nabae, "Instantaneous reactive power compensators comprising switching devices without energy storage components," IEEE Trans. Ind. Applicat., vol. IA-20, pp. 625–630, May/June 1984.

[17] E. Larsen, N. Miller, S. Nilsson, and S. Lindgren, "Benefits of GTO-based compensation systems for electric utility applications," IEEE Trans. Power Delivery, vol. 7, pp. 2056–2063, Oct. 1992.

[18] C. Schauder and H. Mehta, "Vector analysis and control of advanced static VAR compensator," Proc. Inst. Elect. Eng. C, vol. 140, no. 4, pp. 299–306, July 1993.

[19] Y. Zhuang and R. W. Menzies, "Effect of DC capacitance of a STATCOM on the dynamic performance at a weak HVDC terminal," in Proc. 1995, IEEE WESCANEX'95, pp. 289–293.

[20] J. B. Ekanayake and N. Jenkins, "Selection of passive elements for a three-level inverter based static synchronous compensator," IEEE Trans. Power Delivery, vol. 14, pp. 655–661, Apr. 1999.

[21] Y. H. Song and A. T. Johns, "Flexible AC Transmission Systems (FACTS), " ser. Power and Energy, 30. London, U.K.: IEE, 1999.

[22] N. G. Hingorani and L. Gyugyi, Understanding FACTs: Concepts and Technology of Flexible AC Transmission Systems. New York: IEEE Power Eng. Soc., 2000.

[23] G. Strang and T. Nguyen, Wavelets and Filter Banks, Wellesley, MA Wellesley–Cambridge Press, 1996.

[24] F. Moran and D. R. Williams, "Automatic control of power system frequency by machine controllers," Proc. of IEE, vol. 115, no. 4, pp. 606-614, 1968.

[25] I. Daubechies, Ten Lectures on Wavelets. Philadelphia, PA: Society for Industrial and Applied Mathematics, 1992.

[26] J. Shen and G. Strang, "Asymptotics of Daubechies filters, scaling functions, and wavelets," in Proc. of Applied and Computational Harmonic Analysis, vol. 5, pp. 312-331, July, 1998.

[27] G. Strang and T. Nguyen, Wavelets and Filter Banks, Wellesley, MA Wellesley–Cambridge Press, 1996.

[28] J. Upendar, C. P. Gupta, and G. K. Singh, "Discrete wavelet transform and genetic algorithm based fault classification of transmission systems," in Proc. of Fifteenth National Power Systems Conference (NPSC), IIT Bombay, December 2008.

[29] G. Kaiser, A friendly guide to wavelets, 6th Ed., Boston: Birkhäuser, pp. 139-197, 2009.

[30] D. B. Percival and A. T. Walden, Wavelet Methods for Time Series Analysis, Cambridge University Press, 2000, pp. 56-59.

[31] P. F. Ribeiro, "Wavelet transform: an advanced tool for analyzing non-stationary harmonic distortions in power systems," in Proc. of the IEEE International Conference on Harmonics in Power Systems, pp. 365-369, 1994.

[32] C. Blatter, Wavelets: A Primer, A K Peters/CRC Press, 1999, pp. 53-60

[33] K. Lee and M. El-sharkawi, Modern Heuristic Optimization Techniques: Theory and Applications to Power System, Wiley-IEEE Press, 2008, pp. 71-76.

[34] C. Huang, C. Huang, and M. Wang, "A particle swarm optimization to indentifying the ARMAX model for short-term load forecasting," IEEE Tran. on Pow. Syst., vol. 20, no. 2, pp. 1126-1133, May 2005.

[35] Y. Shi and Eberhart, "A modified particle swarm optimizer," in Proc. of IEEE International Conference on Evolutionary Computation, pp. 69-73, 1998.

[36] Y. Shi and Eberhart, "Parameter selection in particle swarm optimization," in Proc. Conference on Evolutionary Programming, San Diego: MIT Press; 1998.

5.0 AN EXPERIMENTAL THREE-PHASE SHORTCIRCUIT FAULT ANALYSIS ON SEIGs FOR DISTRIBUTED WIND POWER GENERATION

5.1 Introduction

One of the challenges in an SEIG system is fault detection in the system. Faults across the high-voltage terminals of the generator lead to economic losses and power outages. A study performed by the Electric Power Research Institute (EPRI) estimated the cost of power interruptions in the US at $119 billion per year [1]. Forced outages are the primary concern of the remote area consumer for causing economic duress. The SEIG is attractive for DWPG as the terminal voltages of the system collapse during short-circuit faults and hence, the excitation of the machine is cut-off driving the machine to just run freely at the wind turbine rotor speed. However, it is necessary for the fault to be detected and communicated to the operator in order to resume operation after fault inspection and clearance.

Generally, when power line fault occurs, the conventional devices such as auto-reclosing circuit breakers or over-current sensors are used to detect the current amplitudes and break the circuit for power transfer termination and safeguard the generator and load. Also, the detection can be communicated to the operator based on the post-fault information gathered.

However, in the case of a SEIG, during three-phase short circuit condition the voltage across the capacitor banks falls to zero and hence the stator current drops to zero. Here the machine is protected from faulty currents as the machine stops generating until the fault is cleared due to zero voltage build up across its terminals. The conventional fault detection devices mentioned above cannot be employed to detect the fault as the amplitudes of currents do not rise for a period of time. Hence, fault detection is necessary through other methods. Fast and accurate fault detection will render immediate corrective action. Thus, it is of vital importance to rapidly detect and identify power system faults, assist the task of repair and maintenance, and reduce the economic effects of power interruption.

This chapter shows this meritorious self-protecting mechanism of the SEIG system

through fault analysis and thus its usability in distributed generation. Also, the wavelet based transient detection scheme which is developed in this thesis for voltage regulation, explained in chapter 4, can be used for fault detection and classification through conditional threshold selection, hence making the wavelet based module a dual purpose module for voltage regulation and fault detection in distributed wind power generation.

5.2 Three-Phase Short Circuit Fault Analysis on SEIGs

Though short circuiting of an SEIG appears to instantaneously de-excite the stator winding, thus causing voltage collapse across the stator terminals, there is a transient state preceding the complete decay of voltage. Hence, a 3-phase short circuit fault has been initiated across the stator terminals of both the aluminum- and copper- rotor machines.

Since the behaviour of the machines is relatively the same, just the study of the behaviour of the machine in general is discussed here.

Figs. 5.1(a), (b) and (c) show the measured results that represent transient behaviour of copper-rotor machine. The negative x-axis shows the pre-fault conditions. The transients are observed on a Tektronix-2024 oscilloscope which has a sampling rate of 2 Giga samples. Analysing the above figures, the most observable phenomenon is the instant decay of voltage across the stator terminals on application of the 3-phase fault. Since the fault is symmetrical, we know it is sufficient to observe any one of the phasors during the fault. Owing to the inductive nature of the machine, the machine opposes the sudden change in current in the circuit, but due to instant collapse of voltage, the current decays almost completely in 0.07 seconds after the fault initiation. However, the current does not completely decay until 0.1s, hence, if the fault is cleared within 0.1s after its initiation, the pre-fault conditions can be regained instantly. In an event that the fault is not cleared within the stipulated time, the SEIG has to re-excite as it has lost its residual magnetism. The re-excitation time does not equal the previous no- load excitation time of the SEIG because of the effects of faults on the residual magnetism of the SEIG which play a pivotal role in the excitation time [2], [3].

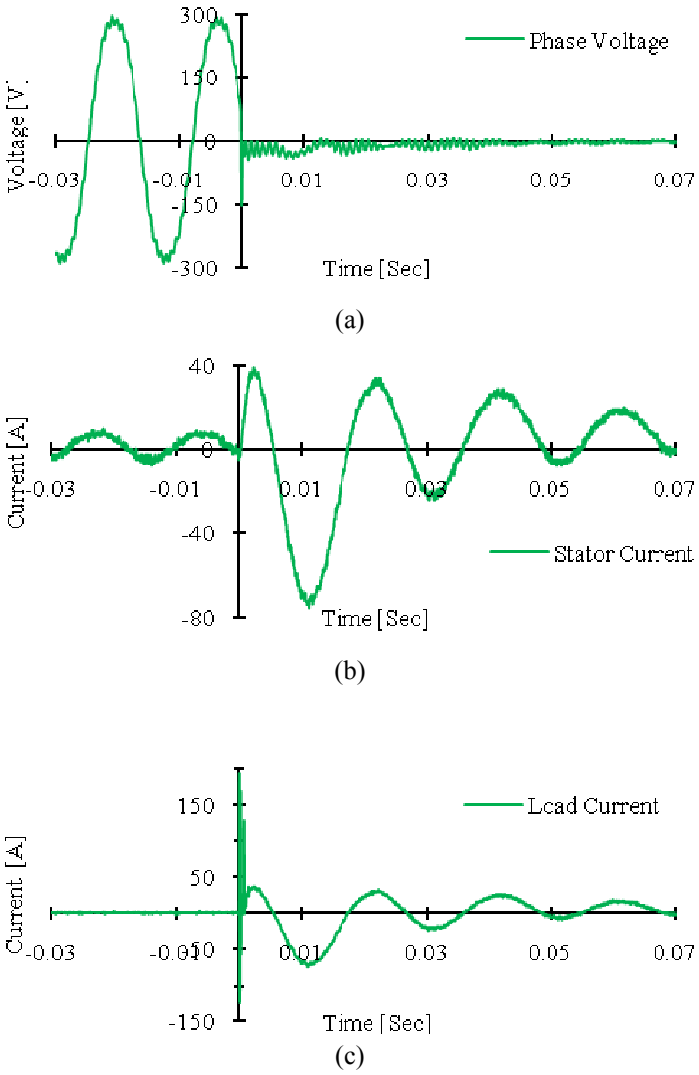

Fig. 5.1. Short-circuit voltage and current profiles of copper-rotor SEIG after fault initiation at the stator terminals. (a) Measured stator voltage. (b) Measured load current. (c) Measured stator current.

The nature of the transients depends on factors such as saturation level, excitation capacitances, discharge times, rotor damping, instant of fault initiation, etc., in the system. Though the decay time of the current in both aluminum- and copper- rotor SEIGs appear to be more or less the same, the nature of transients are observed to be different. As stated earlier in this paper, since the copper-rotor machine has a steeper saturation curve than its aluminum counterpart, decay of current takes relatively lesser time in the copper-rotor machine.

Selecting the filter and threshold wisely, it is possible to integrate a fault detection

function in the wavelet/PSO based VR unit which is applicable for different operating conditions and system parameters. Fault detection unit is separate from main controller and other components of the entire system, hence, will neither be influenced by malfunction of any other units, nor increase computation time of the main controller. It improves the safety and reliability, while maintaining fast response.

5.3 References

[37] N. S. D. Brito, B. A. Souza, and F. A. C. Pires, "Daubechies wavelets in quality of electrical power", in Proc. of 8th International Conference on Harmonics and Quality of Power, 1998.

[38] S. K. Jain, J. D. Sharma, and S. P Singh, "Transient performance of three-phase self-excited induction generator during balanced and unbalanced faults," IEEE Proceedings of Generation, Transmission and Distribution, pp. 50-57, 2002.

[39] R. Wamkeue and I. Kamwa, "Numerical modeling and simulation of saturated unbalanced electromechanical transients of self-excited induction generators," in Proc. of IEEE Canadian conference on Electrical and Computer Engineering, vol.2, pp. 1147-1151, 2000.

6.0 CONCLUSION

It has been an endeavour in this research work, to analyse the performance of conventional 7.5 hp aluminum-rotor induction machine and niche 7.5 hp copper-rotor induction machine as self excited induction generators for distributed wind power generation. A novel two-axis mathematical model of the SEIG has been developed to represent the system using higher order differential equations by means of the stationary reference frame theory. Investigations have been performed using the developed model and calculated results have been compared to the experimental ones. Understanding the inaccuracy of the model, the mathematical model has further been improved by including the include AC conduction effects in the rotor bars of both the machines. Once again numerical investigations on both aluminum- and copper-rotor machines have been performed using this developed model and experimentally verified with results that are obtained from the two 7.5 hp industrial type induction machines. Results obtained using the model by ignoring and also by considering the AC conduction effects in the case of open circuit and static loading conditions have been compared with the experimental ones. For both the machines the models that considered the AC conduction effects produced acceptable results closer in agreement to the experimental results, hence improving the accuracy of the developed mathematical model. Also the AC conduction losses are more in the copper-rotor machine when compared to that of it aluminum counterpart as the skin effect is directly proportional to the conductivity of the material.

As can be seen from the magnetizing curves of each SEIG, the curve for the copper-rotor machine is steeper compared to the aluminum-rotor machine. As a result for the same amount of capacitance the no load output voltage will be higher in case of copper-rotor SEIG. For the same voltage output, a higher value of capacitance will be required for the aluminum-rotor machine.

The voltage and current build up time under open circuit condition is found to be considerably higher in case of the model that ignores the AC effects. It is also observed that the transients decays faster in case of the model that takes AC effects into account.

The CRSEIG could be loaded more than the ALSEIG because of its lower losses, better power factor and hence, has been found to yield higher efficiency. The CRSEIG operates at a slip of 1.05% and the ALSEIG operates at a slip of 1.82% at their maximum

loading conditions, which is lower than the rated slip of the respective machines. It was observed that the no-load excitation requirement of the CRSEIG was a bit more than the ALSEIG. As the machines were loaded the VAR and the capacitance required by the ALSEIG was more than that of the CRSEIG. The range of capacitance requirement for CRSEIG varied from 37μF to 55 μF, whereas the same for ALSEIG varied from 65 μF to 87 μF, for no-load to maximum loading condition. It is also seen that the compensating capacitance requirement of the CRSEIG is reduced due to the design of the machine with higher value of flux density. Otherwise, the lesser capacitance requirement for the CRSEIG can be attributed to the steeper saturation characteristics of the machine.

One of the main drawbacks of a self-excited induction generator is its poor voltage regulation, since there is no separate dc excitation system. The voltage regulation for the aluminum-rotor machine has been found to be better than that of the copper-rotor machine. It is also observed that the for about 6% variation in terminal voltage from the rated value, the CRSEIG, because of its poor voltage regulation, required almost seven steps of capacitor switching to generate the maximum power. Whereas, the ALSEIG required only about four capacitor switching steps to reach its maximum power. Hence, the voltage regulating scheme will be a lot cheaper for the ALSEIG compared to that of the CRSEIG.

It is also observed that the change in frequency for the copper-rotor machine is less than that of the aluminum-rotor machine. Stator frequency of the CRSEIG and ALSEIG dropped to 0.989 pu and 0.982 pu under full load condition, respectively. It is also seen that the copper-rotor machine takes less time to regain a stable frequency during resistive loads and more time than the aluminum-rotor machine at inductive loads.

Furthermore, issues such as voltage regulation and fault analysis in an autonomous distributed wind power generation are elucidated and advantage of the fault tolerant SEIG and the need for fault detection and post-fault data collection in distributed generation is discussed. An exclusive Wavelet/PSO based control algorithm is developed and built on a low cost embedded system for voltage regulation and fault detection. It has been interfaced with a switched capacitor bank to provide an economical and reliable voltage regulation scheme. Results from numerical and experimental investigations are presented.

VITA AUCTORIS

Name : Lakshmi Varaha Iyer

Place of Birth: India

Year of Birth: 1987

Education: 2009 : Bachelor of Technology in Electronics and Communication Engineering, SASTRA University, Thanjavur, India

2005 : Pre-University Degree
Sri Kumaran Public School, Bangalore, India